



# UNIVERSIDAD DE GRANADA

---

Facultad de Ciencias

GRADO EN FÍSICA

TRABAJO FIN DE GRADO

## CINEMÁTICA DE LAS GALAXIAS BARRADAS DE BAJA MASA

Presentado por:

**D. Simon Bonnal de Daniloff**

Curso Académico 2021/2022

## **Resumen**

En este trabajo, tratamos de describir los movimientos de las galaxias de baja masa. Aunque en un principio el trabajo estaba enfocado en galaxias barradas, debido a la baja estadística de este tipo de sistemas en la muestra decidimos ampliar el trabajo al estudio global de galaxias de baja masa. Este tipo de estudio sobre la cinemática de las galaxias ya se ha realizado muchas veces en galaxias más masivas, pero rara vez en galaxias de baja masa. Con tal fin, trabajamos sobre cinco galaxias, de diferentes tipos, y estudiamos sus movimientos rotacionales y no rotacionales gracias a técnicas de análisis espectroscópico. Nuestras conclusiones son que las galaxias de baja masa presentan un disco soportado por una rotación similar a la de las galaxias más masivas. Una vez modelada dicha rotación, la distribución residual de velocidades nos permite analizar los movimientos no circulares y éstos presentan dos tipos principales de patrones: patrones relacionados con efectos a gran escala como pueden ser alabeos del disco (warps) y patrones estocásticos relacionados a escalas locales con formación estelar.

## **Abstract**

In this work, we try to describe the motions of low-mass galaxies. Although at first the work was focused on barred galaxies, due to the low statistics of this type of system in the sample, we decided to extend the work to the global study of low-mass galaxies. This type of study on the kinematics of galaxies has already been carried out many times in more massive galaxies, but rarely in low-mass galaxies. To this end, we work on five galaxies, of different types, and study their rotational and non-rotational motions using spectroscopic analysis techniques. Our conclusions are that low-mass galaxies have a disk supported by rotation similarly to more massive galaxies. Once said rotation has been modeled, the residual distribution of velocities allows us to analyze non-circular movements and these present two main types of patterns: patterns related to large-scale effects such as warps of the disk and stochastic patterns related locally with star formation.

# Contents

<b>1</b>	<b>Introduction</b>	<b>5</b>
<b>2</b>	<b>Theoretical basis</b>	<b>5</b>
2.1	Motions in a galaxy . . . . .	5
2.2	Doppler effect . . . . .	6
2.3	Differential rotation and rotation curves . . . . .	7
2.4	Velocity maps . . . . .	8
2.5	Observational method to obtain velocity measurements . . . . .	9
2.6	Non-rotational motions . . . . .	10
2.7	Previous work . . . . .	11
2.8	Objective of this work . . . . .	11
<b>3</b>	<b><sup>3D</sup>BAROLO</b>	<b>11</b>
<b>4</b>	<b>Data and galaxy sample</b>	<b>12</b>
<b>5</b>	<b>Preliminary calculations</b>	<b>14</b>
5.1	Geometrical parameters . . . . .	14
5.2	Galactic center . . . . .	15
5.3	Recession velocity . . . . .	17
5.4	Isophote fitting . . . . .	18
5.5	Continuum subtraction . . . . .	20
<b>6</b>	<b>Results and discussion</b>	<b>21</b>
6.1	Rotation curves . . . . .	21
6.2	2D residual velocity maps . . . . .	24
6.3	Complementary analysis . . . . .	28
<b>7</b>	<b>Conclusions and future work</b>	<b>29</b>
	<b>References</b>	<b>33</b>
	<b>Glossary</b>	<b>33</b>

## Agradecimientos

*Antes de comenzar este trabajo, quisiera agradecer a las personas sin las cuales no estaría escribiendo estas líneas. Gracias a mis tutoras, Isabel Pérez Martín y Laura Sánchez Menguiano, por su dedicación y pedagogía en la tutorización de este TFG. Durante todas estas largas horas de trabajo, dudas y cuestionamientos, saber que podía contar con su apoyo fue clave y me han permitido enriquecer enormemente mi formación como científico. Gracias también al Dr. Enrico Di. Teodoro, por la ayuda brindada durante la ejecución del software utilizado en el marco de este trabajo.*

*Gracias también a mi familia, tanto del norte como del sur, que siempre me ha apoyado en todos los desafíos a enfrentar. Merci à vous, pour toujours !*

*Finalmente, gracias a mis amigos, por su apoyo incondicional y sus valiosos consejos. Gracias en particular a Marco, Annie y Fidel, quienes siempre han estado a mi lado en los momentos buenos como los difíciles. Gracias también a Gloria Torres, quien me guió durante todo el año con sus consejos y visión más experimentada.*

*¡Muchas gracias a todos!*

## 1 Introduction

One hundred years after the discovery of the first galaxies, our understanding of the Universe has increased considerably. We have gone from the limited vision that all that exists is a few thousand [parsecs](#) away from us, to that of an expanding Universe whose current visible limits are more than 14 billion parsecs away, forming mega-structures that sometimes challenge even the most creative minds.

The kinematics of galaxies is studied since long time and it gives us answers about their formation, their evolution, the material that composes them, the stars present in them, the gas and its multiple interactions and the dynamical processes that make them exist. However, because the Universe has not always been the same and the fact that we have to cope with being, as observers, a part of its ongoing evolution, lots of mysteries still remain. Astronomers and astrophysicists have then developed methods and techniques to try to unveil them and understand the underlying order of the observations.

This first step towards greatness has been made possible thanks to studies on galaxies, which have been improved over the years mostly due to advances in instrumentation, but those on low-mass galaxies, due to the lower luminosity of this type of galaxies, are still very recent. In this bachelor thesis we analyse the motions of five low-mass galaxies with different characteristics and try to determine the origin of those motions, especially non-circular ones, using several techniques.

## 2 Theoretical basis

In this section we describe the theory of motions in galaxies and the tools we use to make the analysis of the data.

### 2.1 Motions in a galaxy

When we observe a galaxy, the light collected with our instruments contains information about the motions of the galaxy projected along our line of sight. The components of these motions are calculated using the [Doppler effect](#) on the emission or absorption lines of the spectrum of the galaxy and their width. The width and the position of these emission lines in the spectrum are affected by different factors such as the expansion of the Universe, local motions of the galaxy in its environment and internal motions.

The expansion of the Universe is observed in what we call the [recession velocity](#) of the galaxy: it is the speed at which an object in the sky recedes from an observer (in this case we are the observer) as a result of the expansion of the Universe. However, when the galaxy is close to a massive object, like another galaxy, its movement in space may not follow the expansion of the Universe since the gravitational pull between both objects affect greatly their respective motions. For example it is the case of our closest neighbour, Andromeda, that is going to collide with the Milky Way in a few billion years ([van der Marel et al., 2012](#)).

On the other hand, galaxies have internal motions that depend on the type of galaxy we are looking at: elliptical galaxies or spiral galaxies; in elliptical galaxies, internal motions are mostly random, causing them to have a shape that resembles that of an ellipsoid. The orbits of their stars can be very elongated, this is why we qualify their [Hubble type](#) from E0 (circular-shaped) to E7 (very elongated).

The internal motions of spiral galaxies are dominated by rotation. Stars move under the influence of gravity, that pull them towards the galactic center, and an effective centrifugal force, pulling them outwards. This is why these galaxies present a flat disk of stars and gas, that strictly follows the rotation induced by the gravitational potential. The disk shows a spiral structure (the spiral arms), which gives name to this type of galaxies. Of course, non-circular and random motions are also present in spiral galaxies; these are the motions that we want to study in this work and the way to do it is by first characterizing the rotational motions and then extracting them from the total motions, resulting in the non-circular motions as velocity residuals. In cylindrical coordinates, rotation can be represented with a vector in the angular direction ( $\theta$ ), and non-rotational motions take place on the vertical ( $z$ ) and radial ( $r$ ) axes.

The total velocity that we observe is a projection of those motions along our line of sight and it can be calculated using the [Doppler effect](#) on the spectrum of the regions of the galaxy. We explain this calculation in the following subsection, but if we divide the galaxy in concentric rings of same width, the observed velocities in our line of sight for each ring ( $V_{los}$ ) can be written as a finite number of harmonic terms ([Franx et al., 1994b](#)). At first order, the expression turns into eq. (2.1):

$$V_{los}(r, \theta, z) = \underbrace{V_{rec}}_{\text{recession motion}} + \underbrace{V_{rot}(r) \cdot \cos(\theta) \cdot \sin(i)}_{\text{rotational motions}} + \underbrace{V_{non-rot}(r, \theta, z)}_{\text{non-rotational motions}}, \quad (2.1)$$

where  $V_{rot}(r)$  is the rotation velocity,  $\theta$  is the azimuthal angle, measured in the plane of the galaxy ( $\theta = 0^\circ$  for major axis),  $i$  is the inclination of the galaxy<sup>1</sup> and  $V_{non-rot}(r, \theta, z)$  the velocity induced by non-rotational motions.

## 2.2 Doppler effect

In order to study the kinematics of galaxies from their spectra we can measure velocities applying the [Doppler effect](#) on any spectral line (in emission if we analyse the ionised gas or in absorption if we study the stellar populations). The Doppler effect is the change in frequency of the emission of a moving source. This phenomenon appears for all kind of waves, but here we are interested in electromagnetic waves. The light we are receiving from astronomical objects is potentially shifted towards lower wavelengths (i.e. blueshifted) if they are approaching, or higher wavelengths (i.e. redshifted) if they are recessing. This displacement of the spectrum can then be converted into velocity in our line of sight,  $V$ , using the difference of frequencies or, in our case, wavelengths, and equation (2.2).

$$z = \frac{\lambda_{obs} - \lambda_{rest}}{\lambda_{rest}} = \frac{V}{c}, \quad (2.2)$$

where  $z$  is the so-called [redshift](#),  $\lambda_{obs}$  is the observed wavelength of a specific spectral line from the spectrum of the astronomical object,  $\lambda_{rest}$  the wavelength measured in laboratory and  $c$  is the speed of the light in vacuum. In this work, the spectra of the galaxies will be redshifted because the recession is dominant due to the expansion of the Universe (what we call the [Hubble flow](#)).

<sup>1</sup>It is the angle between the line perpendicular to the plane of the galaxy and the line of sight; the inclination of a galaxy is later discussed in § 5.1.

### 2.3 Differential rotation and rotation curves

Once the [recession velocity](#) is taken into account from the expression 2.1, the remain orbital velocity will be mainly governed by the rotation of the galaxy. When we observe the rotation of the disk of a spiral galaxy, we do not observe a solid body rotation but a differential rotation. This means that, although all the disk from a certain radius rotates at a similar speed, because outer stars are further from the galactic center, it requires for them more time to complete a full orbit ([Shu, 1982](#)).

In order to visualize the rotation velocity of a galaxy, we use a line-of-sight position-velocity diagram, that represents the velocity of the disk in our line of sight ( $V_{los}(r)$  —or  $V_{rot}(r)$ , dividing  $V_{los}(r)$  by  $\sin(i)$ —) as a function of the radial distance from the center of the galaxy ( $r$ ). This type of representation is commonly called a *rotation curve*.

If we know the mass distribution of the galaxy,  $M(r)$ , we can easily determine the rotation velocity of any object at distance  $r$  from the center using Newton’s gravitational law and the centripetal force:

$$F = \frac{GMm}{r^2} = \frac{mv^2}{r} \implies v = \sqrt{\frac{GM(r)}{r}}. \quad (2.3)$$

We usually model the mass distribution by an exponential disk (model first proposed in [Freeman \(1970\)](#) for spiral galaxies), so the rotation curve we would expect to be observed would start at the center being null, then grow rapidly since the mass increases quickly due to the high density near the center, it would eventually reach a maximum value and then decrease slowly as  $v \propto r^{-1/2}$ . However, this is not what is observed experimentally and rotation curves do not drop off after reaching the maximum value, but stay flat as the distance increases. These re-

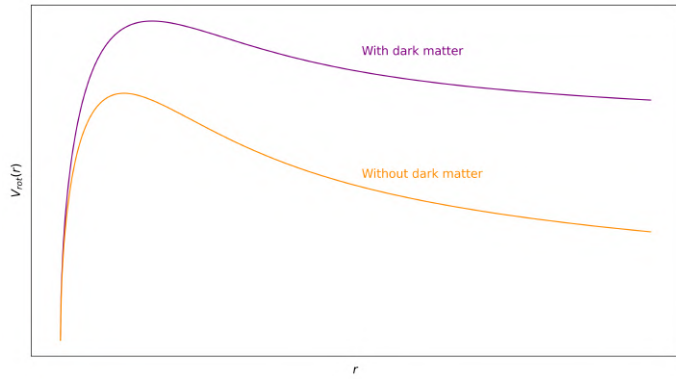


**Figure 1: Example of rotation curves.** The orange curve is the rotation curve obtained for the Newtonian model with only baryonic mass, while the purple curve also includes a component for [dark matter](#), following the model describe in [Wojnar et al. \(2018\)](#).

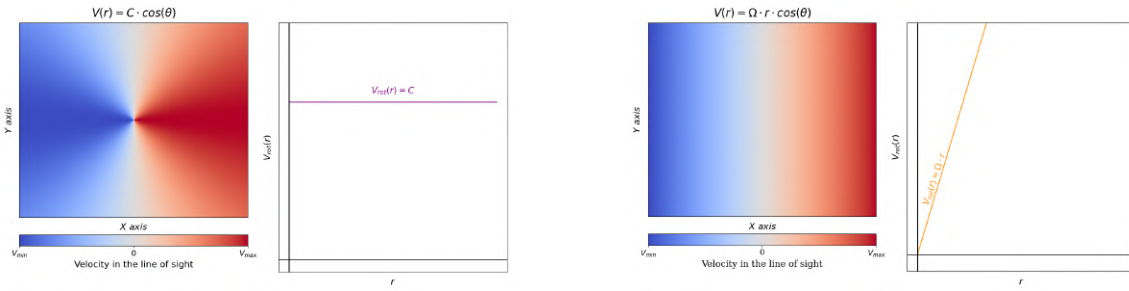
sults, presented by Rubin, Ford and Thonnard in 1980 ([Rubin et al., 1980](#)), can be explained as follows: whether a relevant part of the mass of the galaxy is invisible and located at large radii, flattening the rotation curve (this “[dark matter](#)” is the hypothesis advanced in [Rubin et al. \(1980\)](#)), whether a modified version of Newtonian gravity has to be applied at large radii (we call this type of theories MODified Newtonian Dynamics, [MOND](#)). An example of the expected rotation curve (without dark matter) and the one we observe (with dark matter) can be seen in Fig. 1.

Nowadays, we know that dark matter and MOND theories show good results but also important issues ([Sellwood and Kosowsky, 2001](#); [Sanders and McGaugh, 2002](#)) and we hope to be able to find new evidences that might help to determine which one of them (or other theories) is correct. In this work we will study the kinematics of galaxies under the prism of the  $\Lambda$ DCM model, which states the existence of dark matter.

## 2.4 Velocity maps

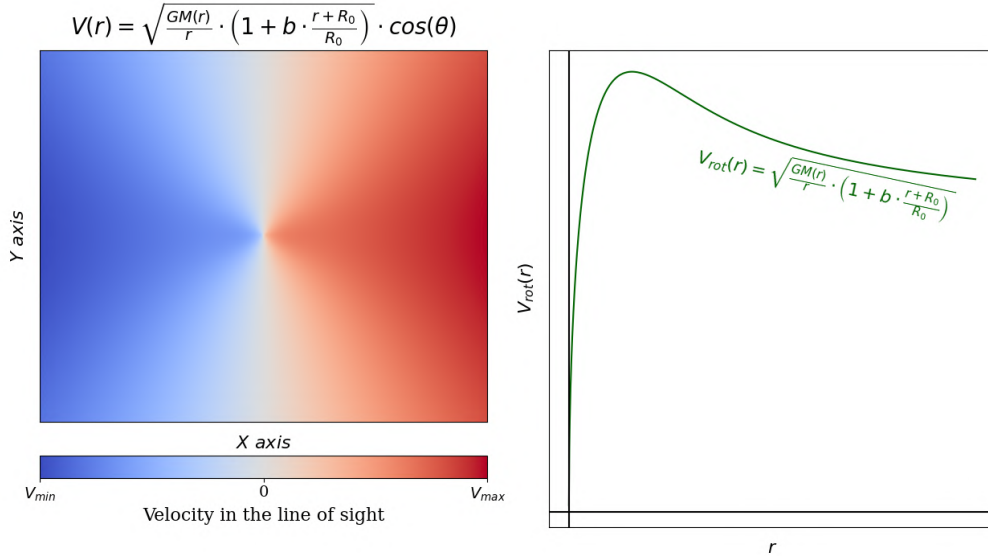
Velocities in our line of sight can also be represented using 2D maps by calculating the velocity of each region of the galaxy: this representation is called a **velocity map**. It can tell us which side of the galaxy is receding and which one is approaching, but can also give us information about the dispersion in the velocities of the gas<sup>2</sup> ( $\sigma_{gas}$ ) or, once the rotation is removed, the non-circular motions.

The trend followed by  $V_{los}(r)$  and showed in § 2.3 can be modelled using a rigid body-rotation velocity,  $V_{rot}(r) = \Omega \cdot r$ , near the center and a constant rotation velocity,  $V_{rot}(r) = C$ , at larger radii. In Fig. 2 three examples of rotation curves, generated from the constant and proportional models and a combination of them, and associated velocity maps, are shown.



(a) Constant rotation velocity,  $V_{rot}(r) = C$ .

(b)  $r$ -dependent rotation velocity,  $V_{rot}(r) = \Omega \cdot r$ .



(c) Rotation velocity from Wojnar et al. (2018),  $V_{rot}(r) = \sqrt{\frac{GM(r)}{r}} \cdot \left[1 + b \cdot \left(1 + \frac{r}{R_0}\right)\right]$ .

**Figure 2: Examples of rotation curves and velocity maps.** We represent three types of rotation curves and the velocity maps associated with each one. As we can see, the model used in 2c is a combination of the first two, where the rotation corresponds to a solid-body motion for low  $r$  and to a constant rotation for large  $r$ . We used the model describe in Wojnar et al. (2018).

<sup>2</sup>This dispersion show how scattered are the values of the velocities of neighbour regions. High dispersion means that processes make the gas have different velocities in near regions of the galaxy.

## 2.5 Observational method to obtain velocity measurements

Now we know what to expect observing the velocities within a spiral galaxy. But what is the subject whose velocities come from?

As we said previously, galaxies contain stars, dust and gas. Different components can be used in order to study motions, but here we calculate the motions of the gas, which is mostly composed of hydrogen. Depending on the conditions of the interstellar medium (ISM), such as the temperature and the density, hydrogen can be in a molecular, (neutral) atomic (denoted HI) or ionized (HII) state (Ferrière, 2001). In the first case we can detect it using radio and infrared light, in the second case using the 21-cm absorption line and in the ionized case we use the  $H\alpha$  emission line. The molecular clouds, where star formation may be occurring, are primarily located in the galactic discs (and following the spiral arms); the hydrogen atomic gas is seen in the galaxies to radii much larger than the visible light (see Fig. 3); and the  $H\alpha$  emission is typically seen in hot environments like star-formation regions or simply around hot stars that ionize the gas around it. (Shu, 1982)

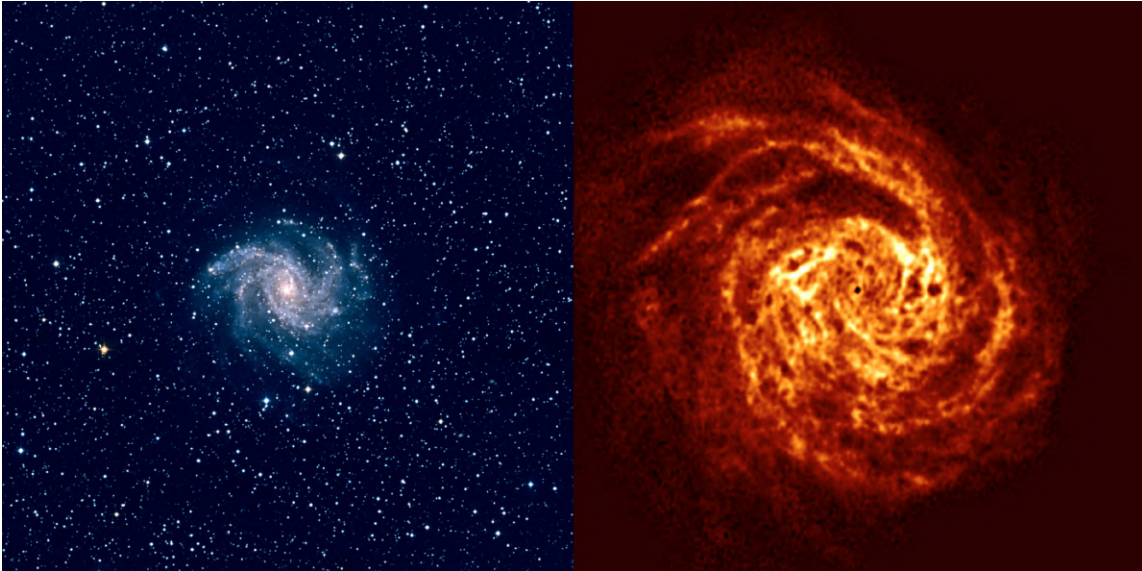


**Figure 3:** Optical (left) and radio (right) images of the galaxy NGC 6946 from Boomsma et al. (2008) at the same scale.

The HI cold gas covers the majority of the interstellar medium and we recently discovered that we could use it to observe star formation far beyond the optical radius of galaxies (Verdes-Montenegro et al., 2015), making it a lot more useful than ionized gas when we want to study the most distant parts of the disk<sup>3</sup> (of course, in practice, it also depends on the quality of the data). So in order to calculate the velocity at the flat part of the rotation curve, from now on called  $V_{flat}$ , we can use the 21-cm spectral line of HI gas: because HI gas covers the disk at larger radii than ionized gas it allows to better trace the outer parts of the disk and determine more easily the distance at which the rotation curve flattens.

<sup>3</sup>In this bachelor thesis we use the ionized gas for our analysis because we want to study the entire disk, not only its outer parts, and because it can provide more precise results than HI gas, which is necessary when the objective is to study local motions in a galaxy.

We can estimate  $V'_{flat}$ , which is  $V_{flat}$  projected onto the line of sight ( $V'_{flat} = V_{flat} \cdot \sin(i)$ ), by searching in a flux density-velocity graph (representation of the flux density of the luminous material in the galaxy as a function of its velocity) the maximum values: since the stars located at a distance from the center greater than a certain radius have a speed similar to  $V'_{flat}$ , their fluxes add up and this creates a maximum on the graph at  $V = |V_{rec} - V'_{flat}|$ . This value can then be calculated using the value of the mean parameter  $\mu$  of gaussian fits. In the case of a single peak emission, we use the FWHM since  $V$  is too close to  $V_{rec}$  in the flux density-velocity graph. In Fig. 4 we show the flux density-velocity graph for an **edge-on** galaxy (where its inclination with respect to our line of sight is close to  $90^\circ$ ).

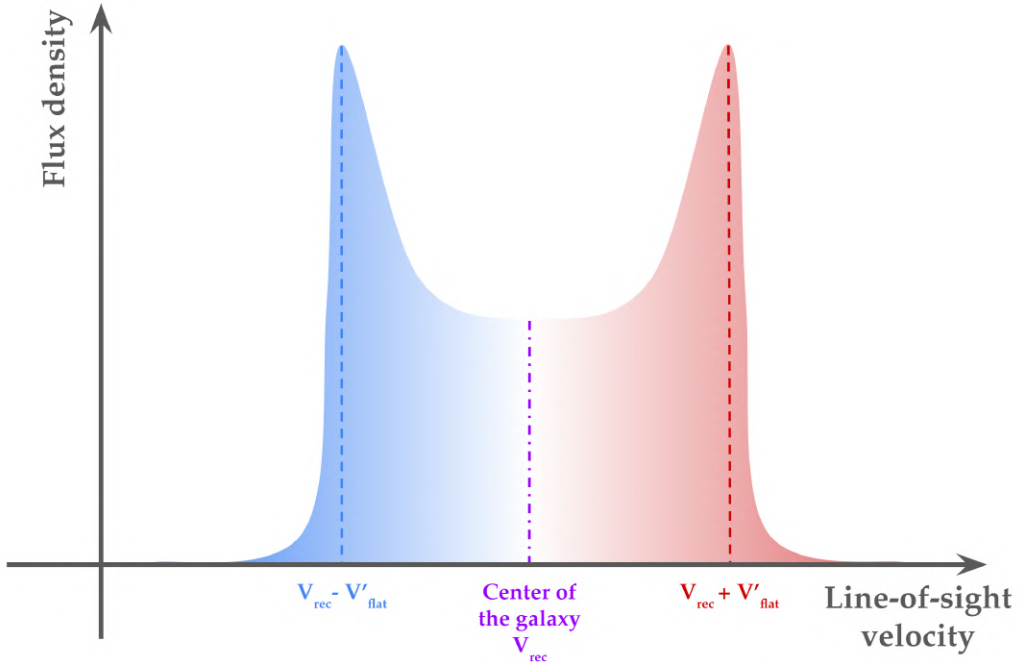


**Figure 4: Example of the flux density-velocity graph of an edge-on galaxy.** We also show how  $V'_{flat}$ , which is  $V_{flat}$  projected onto the line of sight, can be calculated using the position of the maxima.

## 2.6 Non-rotational motions

Internal non-rotational motions in a galactic disk can be induced by many processes. Here we show a variety of types of non-circular motions (Bosma, 1978):

- Associated with spiral arms: they are directly induced by the presence of the arms of the galaxies and create asymmetric motions.
- Large scale symmetric deviations: when the elliptic shape of the disk has different orientations at different radii, but the velocity maintains its central symmetry. If this variation is created in the outer parts of the galaxy, we say that the plane of the galaxy is “warped”.
- Large scale asymmetries: they appear in the outer parts of galaxies due to interactions with other neighbouring galaxies.
- Small scale asymmetries: they are more irregular and can have different origins.

In addition to these, we have to take into account the fact that the model used to determine circular motions can produce discrepancies in the results, because we cannot assess the effects of non-circular motions: for example, allowing the orientation of the disk (called position angle) or inclination to vary from ring to ring may cause the non-circular motions to be masked (Sanchez, 2009).

In general, any perturbation of the gravitational potential may produce these non-circular motions, from the mix of gases with different torques or viscosities to the bar a galaxy may have in its center (Di Teodoro and Peek, 2021) or even the gas ejected in the regions of star formation. This is why characterizing them is complicated.

## 2.7 Previous work

Much work has been carried out to study global kinematics of spiral galaxies (Teuben, 1991; Franx et al., 1994a; Schoenmakers et al., 1997), but dependence on different parameters and analysis of low mass galaxies is currently an active field of research.

Until not so much, we did not know much about the kinematics of low-mass galaxies, like if they presented a disk supported by rotation or not. Nowadays we know they rotate, however non-rotational motions are still being studied.

Many analyses are carried out with the help of simulations so we are not limited by the intrinsic difficulties faced during their observation, like their low luminosity. Simulated barred galaxies seem to show different non-circular motions are due to the bar's orientation (Rhee et al., 2004; Valenzuela et al., 2007); in the case where the dark matter halo is included in the simulation, this one affects the shape of the gravitational potential and, therefore, may induce changes in the rotation too (Marasco et al., 2018; Oman et al., 2019); finally, non-circular motions tend to be underestimated in low-mass galaxies and results show this underestimation provokes models to fail in describing correctly the rotation and they need to be reviewed in order to fit better the kinematics of low-mass galaxies (Spekkens and Sellwood, 2007). As observational techniques improve, as well as modeling and simulations, more details about spiral galaxies' rotation are discovered.

## 2.8 Objective of this work

In this bachelor thesis we extract and study the non-circular motions of low-mass galaxies. Although at first the work was focused on barred galaxies, due to the low statistics of this type of system in the sample, we decided to extend the work to the global study of low-mass galaxies.

We will fit the rotation of the galaxies using the  $H\alpha$  emission line and try to determine the residual motions that compose their velocity fields. We will then use different methods in order to determine the origin of these motions.

## 3 <sup>3D</sup>BAROLO

<sup>3D</sup>BAROLO is the software we use in order to derive the rotation curves of the galaxies we study. It is a software developed by E.M. Di Teodoro and F. Fraternali that determines the rotation curve of spiral galaxies from emission-line observations (Teodoro and Fraternali, 2015).

This goal is achieved by generating and comparing 3D tilted-ring models of the thin disk of the galaxy of interest, assuming  $V_{rot}$  constant. The [tilted-ring model](#) (Rogstad et al., 1974) is based on the assumption that the emitting material is inside a thin disk, that its motions are dominated by the rotation of the galaxy, and that each ring at each radius has a constant circular velocity that only depends on its distance from the center. <sup>3D</sup>BAROLO builds a number of models using Monte Carlo method as artificial 3D observations and compares them with the input cube, finding the geometrical and kinematical parameters that better fit the data. What makes <sup>3D</sup>BAROLO really unique is the fact that unlike traditional methods that mostly apply to 2D velocity fields (e.g., [Beegman, 1987](#); [Spekkens and Sellwood, 2007](#)), it applies tilted-ring model and performs the fits of these models directly on data with 2 spatial dimensions and 1 spectral dimension (these data are called [data cubes](#)). This is why having data cubes of the galaxies with good resolutions in space but also in spectral coordinates is necessary. A great advantage of a software like <sup>3D</sup>BAROLO is its ability to work with any emission line of a spectrum, making it a versatile instrument able to get the rotation curves of galaxies from HI observations to CO, C<sup>+</sup>, H $\alpha$ , [NII] and [OIII] spectroscopic lines, i.e., from observations in various ranges of the electromagnetic spectrum. In this work we use the H $\alpha$  line, because the ionization processes that excite this line occur all over the disk of the galaxies. This makes H $\alpha$  one of the brightest and easiest to observe emission lines across the whole galaxy extension available in the optical spectral range.

This tool is especially useful for high-resolution data, but one must be careful with the combination of four factors: the inclination of the galaxy disk, the spatial resolution, the spectral range and the S/N ([signal-to-noise ratio](#)). These parameters have to be accurately determined in order to get good results from <sup>3D</sup>BAROLO. In particular the effect of the inclination is noticed to be very important, especially in the case of dwarf galaxies ([Teodoro and Fraternali, 2015](#)).

<sup>3D</sup>BAROLO models the rings along the disk using four velocities: the recession velocity,  $V_{sys}$ , the rotation velocity,  $V_{rot}$ , the radial velocity,  $V_{rad}$ , and the gas velocity dispersion,  $\sigma_{gas}$ . Each of them can be considered as “free” and be fitted, or can be stated as “fixed” and then not be fitted; in all the cases, an initial guess has to be given to the software for all the parameters, even the geometrical parameters (these are the position angle, inclination and galactic center position, and are explained in § 5.1). The more accurate these estimations are, the better the results will be.

## 4 Data and galaxy sample

In this section we explain which observational data were chosen for this work. In order to study the kinematics of spiral galaxies, we need data that cover all their disks and that contain spectroscopic information, since we use spectral lines to determine the velocities. This type of data are obtained using integral field units (IFU). IFUs are used to study extended source of light such as galaxies applying a technique called integral field spectroscopy (IFS), that can be resumed as follows: the light received from each pixel of the field is analysed by a spectrograph and stored as a spectrum. All the spectra are then stacked in a [data cube](#), a file with two spatial dimensions and one spectral dimension.

Nowadays, one of the best instruments that generate this type of data is MUSE (Multi Unit Spectroscopic Explorer), mounted on the Very Large Telescope (VLT) of the European Southern Observatory (ESO) (Bacon et al., 2010). It is for this reason that we have decided to select our galaxies from the AMUSING survey (now AMUSING++, López-Cobá et al., 2020), as it provides a large sample of high quality spectral cubes obtained with MUSE. This instrument has very good spectral range (from 1750 at 4650 Å to 3750 at 9300 Å) and spatial resolution (pixel scale: 0.2 arcsec). The AMUSING++ data gathers 600 hours of observations during which more than 600 galaxies were observed, having a mass between  $10^8$  and  $10^{12} M_{\odot}$  and located at a distance between 0.8 and 420 Mpc ( $0.0002 < z < 0.1$ ).

We selected galaxies from the AMUSING++ catalogue based on the mass: we want low-mass galaxies so we chose a mass limit of  $10^9 M_{\odot}$ . This limit is commonly taken to separate massive galaxies from low-mass ones and, as a reference, it is a thousand times smaller than the mass of our own galaxy, the Milky Way.

Due to the time limitations of the present work, we have constrained our analysis to five representative galaxies from the initial sample that fulfilled our selection criterion from the AMUSING++ catalogue. In Fig. 5 we show them: CGCG 067-014, UGC 10023, KUG 1201+220, SDSS J164711.10+210527.0 and CGCG 012-116. In Tab. 1 we also show their known characteristics.

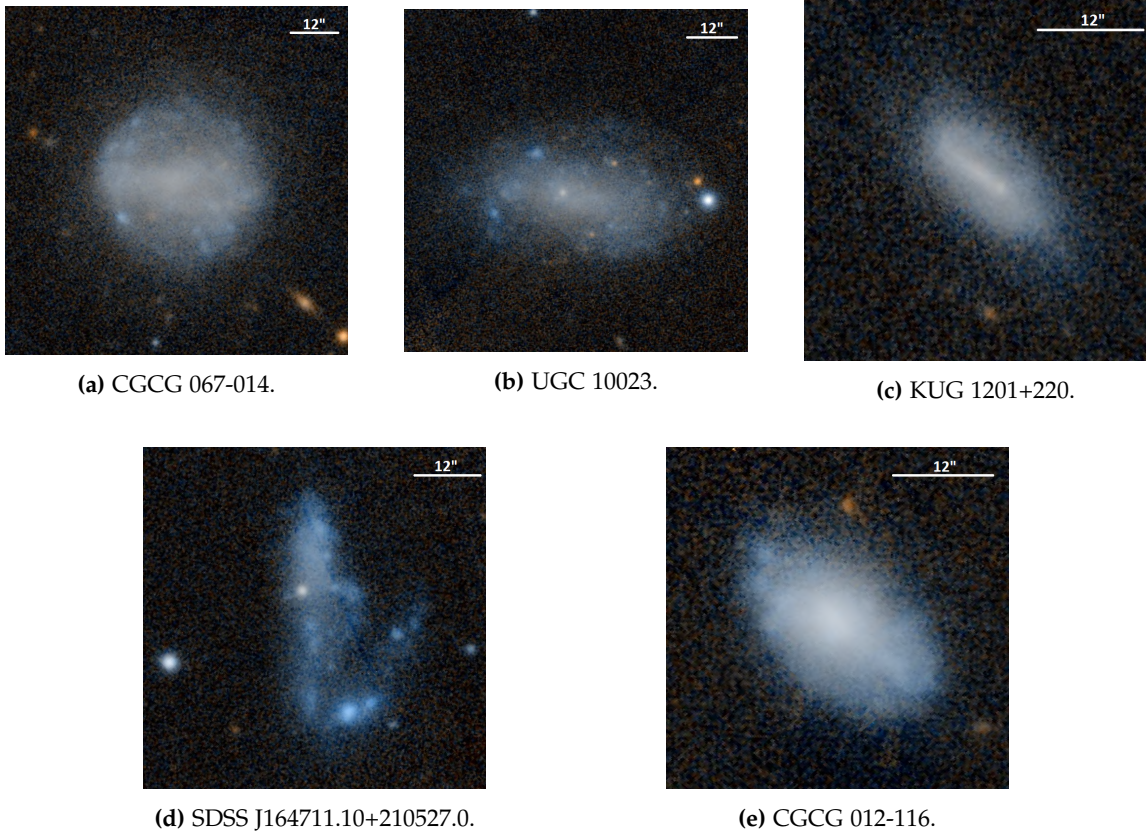


**Figure 5: Images of the five galaxies analysed in this bachelor thesis.** All these images have been exported from the ALADIN interactive sky atlas (Bonnarel et al., 2000) using the data obtained by the Pan-STARRS (DR1) survey (Chambers et al., 2016).

**Table 1: Main properties of the five galaxies analysed in this bachelor thesis.** All the information was extracted from NASA/IPAC Extragalactic Database (NED) except the redshift that was obtained from AMUSING++ survey.

Name	RA (J2000)	Dec (J2000)	Stellar mass ( $\log(M_*/M_\odot)$ )	Distance (Mpc)	Redshift
CGCG 067-014	11h 09m 23.310s	10° 50' 02.70"	8.79	28.14 ± 2.00	0.00517
UGC 10023	15h 46m 09.724s	06° 53' 54.50"	8.40	22.64 ± 1.59	0.00466
KUG 1201+220	12h 04m 16.490s	21° 47' 52.70"	8.66	99.52 ± 6.97	0.02148
SDSS J164711.10+210527.0	16h 47m 11.106s	21° 05' 27.06"	8.46	39.6 <sup>†</sup>	0.00881
CGCG 012-116	11h 55m 04.907s	01° 43' 11.32"	8.37	24.49 ± 1.75	0.00439

<sup>†</sup> This value is obtained from [Privon et al. \(2017\)](#).

## 5 Preliminary calculations

Now that we are familiar with the data, we must prepare them in order to properly derive the galaxy rotation curves.

### 5.1 Geometrical parameters

We will first characterize the geometry of the disk of the galaxies we study through a series of parameters.

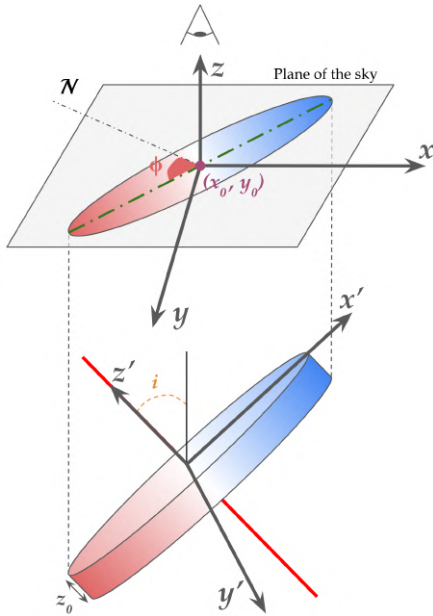


**Figure 6: Visual description of the parameters of the galaxy: inclination ( $i$ ), center ( $x_0, y_0$ ) and position angle ( $\phi$ ).** We also added the width of the disk of the galaxy,  $z_0$ . We used red and blue colors in order to show the rotation (red side is recessing, blue side is approaching).

The disk of a galaxy also has a width, here called  $z_0$ , but it is common to consider an infinitely thin disk ( $z_0 \sim 0$ ). This approximation is made in order to facilitate the calculations and it will not suppose a great change in the results since the distances along the plane of the galaxy are a lot larger.

Working on distant objects like galaxies, we also have to remind ourselves that we cannot change our physical perspective on the subject of the study, we cannot rotate the galaxy, approach to it or isolate it from the rest of its environment; that is why we also have to take into account fundamentals parameters like the inclination of the galaxy ( $i$ ), its position in the sky ( $x_0, y_0$ ) and what we call the position angle ( $\Phi$ ).

The inclination of a galaxy is the angle between the line perpendicular to the plane of the galaxy and the line of sight. The position of a galaxy is defined by its center, and here ( $x_0, y_0$ ) are the right ascension (RA) and the declination (DEC) of this point of the sky. Finally, the position angle is the angle that identifies the position of the major axis on the preceding half of the galaxy and it is taken counterclockwise from the north direction. In Fig. 6 we show a scheme of these parameters.

The inclination of the galaxy is the most critical parameter, because as we saw in eq. 2.1, it directly impacts the value of the observed velocity (if  $i$  is too low, the motions that occur within the plane of the disk will not be visible); then, we talk about “face-on”, “edge-on” or “intermediate” inclination of the galaxies. Fig. 7 shows the projection of the rotation velocities of a galaxy in each case:

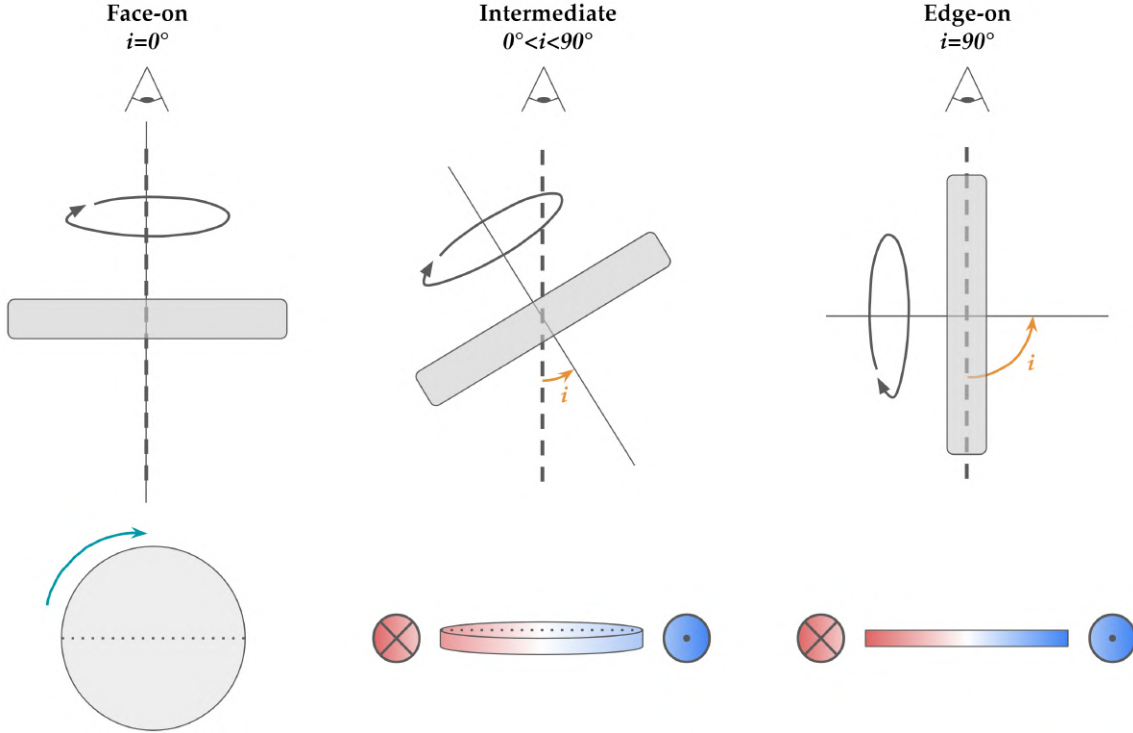


**Figure 7: Possible inclinations of a (circular-shaped) galaxy.** Face-on (left):  $i = 0^\circ$ , rotational motions occur in a plane perpendicular to the line of sight so we cannot detect them. Intermediate (center):  $0^\circ < i < 90^\circ$ , in this case we see the galaxy with a certain inclination and we are able to detect motions occurring in the plane. Edge-on (right):  $i = 90^\circ$ , we see the galaxy as edge-on, so all the velocities occurring within the plane of the galaxy can be projected on our line of sight and the term of the rotation velocity is maximum. On the second row we added how the galaxy would be seen from the observer perspective, using red and blue colors in order to show the rotation (red side is receding, blue side is approaching).

The inclination is directly related to the ellipticity of the ellipse projected on the plane of the sky:  $\cos(i) = \frac{b}{a} = 1 - e$ , where  $b$  is the length of the minor axis,  $a$  is the length of the major axis and  $e$  the ellipticity.

In the following subsections we will determine all these geometrical parameters and the recession velocity, of which we already talked about in § 2.1, for all the galaxies.

## 5.2 Galactic center

We first need to determine the galactic center of the galaxies in order to provide it as an input parameter for <sup>3D</sup>BAROLO.

In order to calculate the galactic centers, which would correspond to the optical nucleus of the galaxies, we use an image of the stellar continuum from the **R band**, at  $(658 \pm 138)$  nm.

We first make an estimation of the galactic center using coordinates from AMUSING++ survey, then create a window of  $10 \times 10$  pixels around it and fit it with a symmetric two-dimensional gaussian function: the peak of light would be the central point of the function and our galactic center. In the case of SDSS J164711.10+210527.0, which is a highly distorted galaxy, because the central point defined by AMUSING++ is for the whole system (including the other galaxy interacting), we estimated by hand the galactic center and then fit the window around it.

In Fig. 8 galaxies' centers are shown.

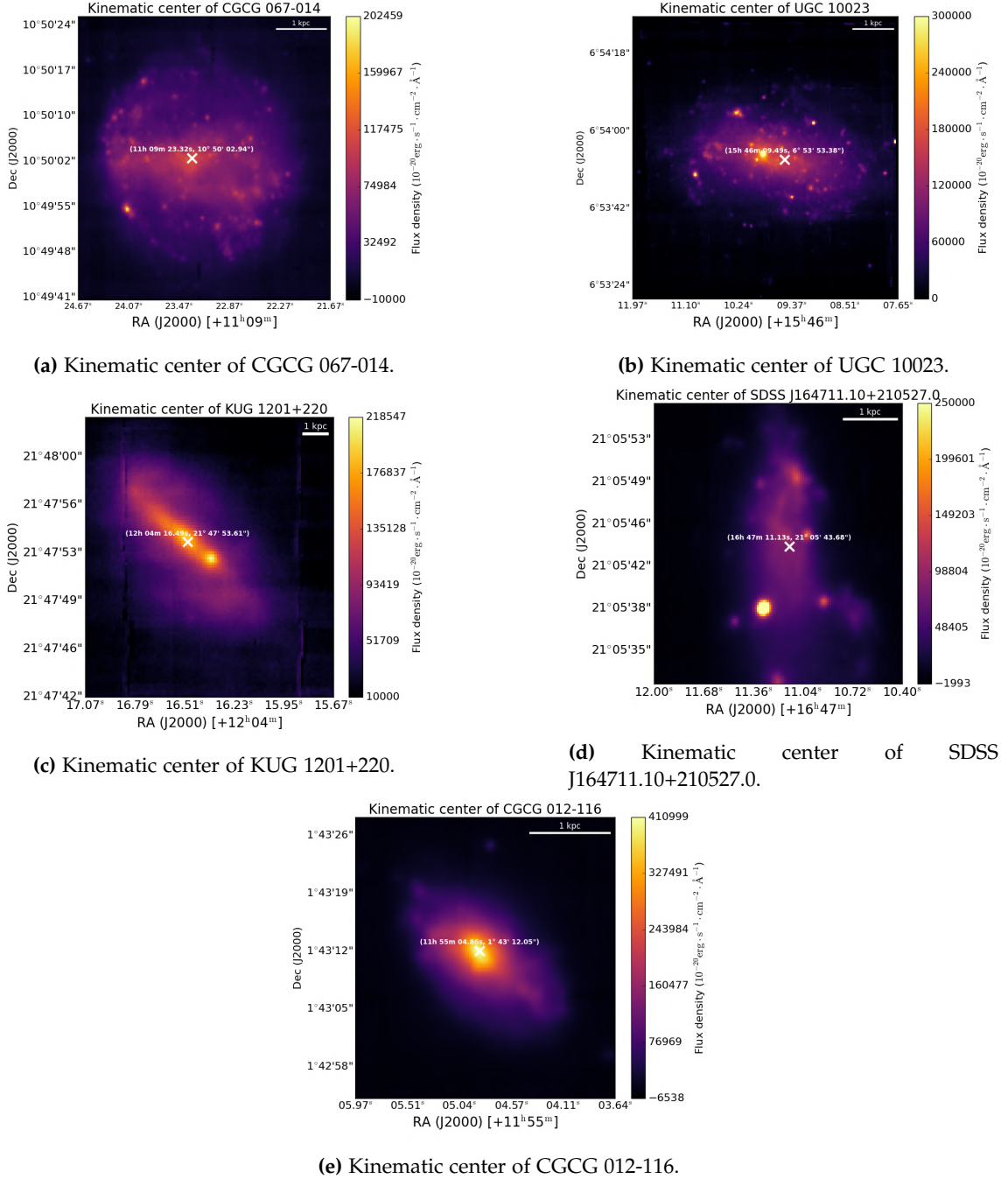
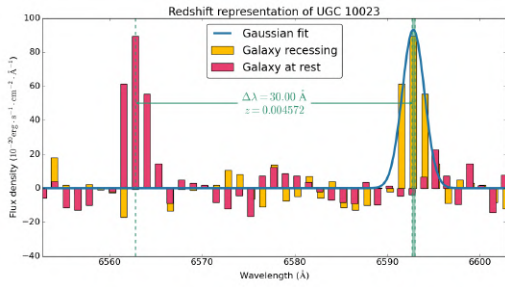


**Figure 8: Kinematic centers of the five galaxies.** We represent the center of each galaxy found using the photometric center with the R band.

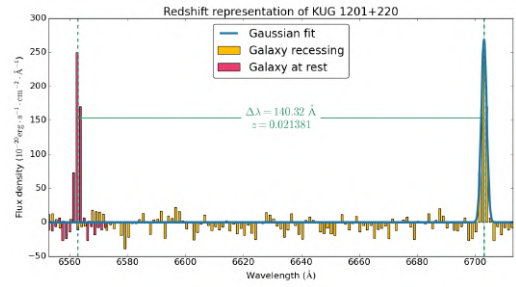
### 5.3 Recession velocity

We are now looking for the recession velocity of the galaxies, the speed at which the galaxies are moving away from us. For that we use the Doppler redshift of the  $H\alpha$  emission line, since it is generally the most intense line in the spectra. We use the spectra of spaxels that are near the center since their redshift should not have any other major source but the recession motion of the galaxy (the center of the disk does not rotate); we use all the spaxels within a square of  $2''$ -side around the galactic center in case  $H\alpha$  is not detected in the central spaxel. To avoid misdetections we also restrict our search to those spectra which  $H\alpha$  amplitude is greater than three times the standard deviation of the continuum of the spectrum. In the case of CGCG 064-014, there are no spaxels fulfilling these criteria and, therefore, no redshift estimation has been made. We decided to use then the value provided by the AMUSING++ survey since those of the rest of the galaxies agree very well with our estimations (see below).

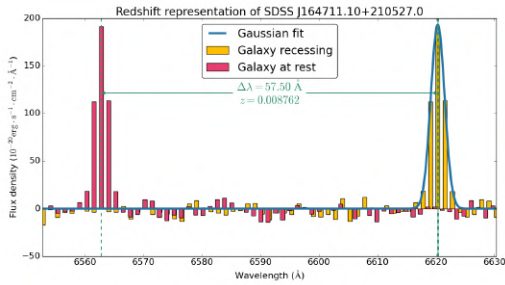
Once we find the  $H\alpha$  line in each spectrum, we fit it with a gaussian function and estimate the redshift using the eq. 2.2, knowing that the wavelength rest of this line is  $\lambda_{rest} = 656.279 \pm 0.003$  nm. The results of those fits are shown in Fig. 9 and Tab. 2.



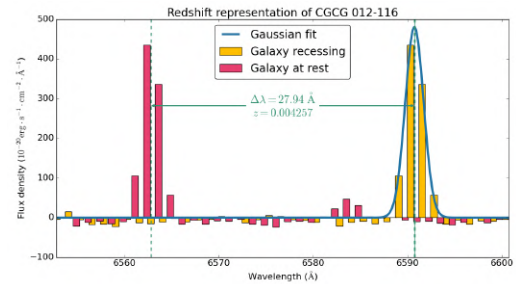
(a) Redshift representation of UGC 10023.



(b) Redshift representation of KUG 1201+220.



(c) Redshift representation of SDSS J164711.10+210527.0.



(d) Redshift representation of CGCG 012-116.

**Figure 9: Redshift representations of four galaxies.** In each subfigure we represent the spectrum of the galactic center of the galaxy around the  $H\alpha$  line. This spectrum is shown without modifications in yellow, at rest in pink (redshift corrected) and we also show the gaussian fit applied in each case in blue. The fit of CGCG 064-014 is not present because of the absence of emission lines in its central region, preventing us to make a proper fit.

All the emission lines are redshifted, and KUG 1201+220 presents the higher redshift, up to five times higher than the redshifts of the other galaxies. In the case of CGCG 064-014, because we could not calculate the redshift properly, we decided to use the one provided by the AMUSING++ survey as a reference value.

**Table 2: Derivation of the redshift for the galaxies using the  $H\alpha$  emission line.** Each value has an error calculated using the uncertainty of the parameters of the fits. We also calculated the relative error committed in reference to the redshift provided by the AMUSING++ survey. The galaxy CGCG 064-014 does not have any experimental value due to the absence of emission lines in the central zone of the galaxy; its redshift and recession velocity are obtained directly from the AMUSING++ survey.

Galaxy	$\lambda_{obs}$ (Å)	$\lambda_{obs} - \lambda_{rest}$ (Å)	$z_{exp}$ [ $\Delta_{rel}$ ]	$V_{rec}$ ( $km \cdot s^{-1}$ )
CGCG 067-014	-	-	0.005175	1551.4
UGC 10023	$6592.80 \pm 0.15$	$30.00 \pm 0.15$	$0.004572 \pm 0.000023$ [1.991%]	$1371 \pm 7$
KUG 1201+220	$6703.12 \pm 0.06$	$140.33 \pm 0.06$	$0.021381 \pm 0.000009$ [0.476%]	$6409 \pm 3$
SDSS J164711.10+210527.0	$6620.30 \pm 0.05$	$57.50 \pm 0.05$	$0.008762 \pm 0.000007$ [0.596%]	$2626.8 \pm 2.1$
CGCG 012-116	$6590.737 \pm 0.023$	$27.937 \pm 0.023$	$0.004257 \pm 0.000004$ [2.953%]	$1276.2 \pm 1.1$

#### 5.4 Isophote fitting

The last step is to find the position angle (PA,  $\Phi$ ) and the inclination ( $i$ ).

In order to estimate these values, we use the method called [isophote fitting](#). It consists in using an image of the galaxy at a specific wavelength (here we compute an image integrating the spectral axis over a known continuum passband) and to trace ellipses around the center of the galaxy following the light distribution. We then fit these ellipses to galaxy isophotes, curves of equal brightness, with an algorithm ([Jedrzejewski, 1987](#)) to estimate the ellipticity and position angle over the disk of the galaxy. In Fig. 10 we show an example of isophote fitting with one of our galaxy.

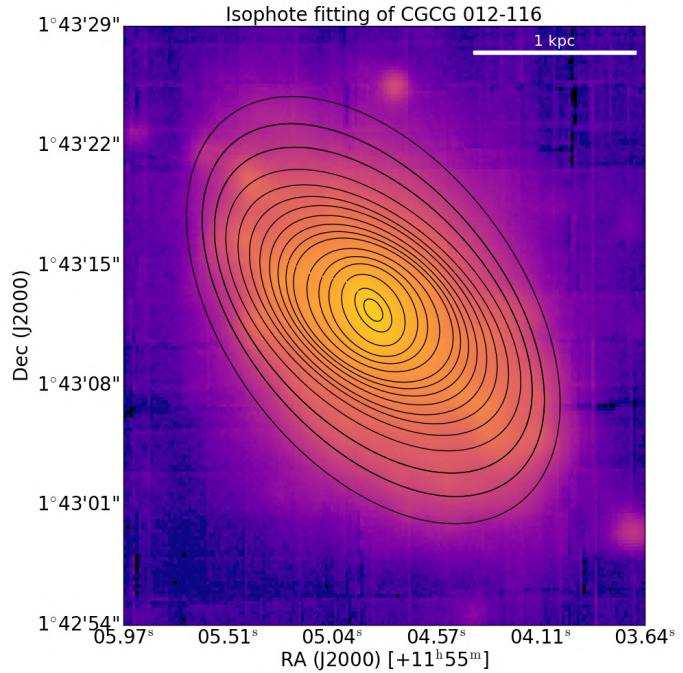


**Figure 10: Representation of the isophote fitting of CGCG 012-116.**

Because all those parameters are not fixed along the disk (the galaxy presents irregularities that affect the surface brightness of the image used for the fits, such as a central bar, denser regions of material, etc.), we only use the isophotes of the outer regions of the galaxy as in these regions the contribution of the galactic disk dominates the emission.

We apply the `isophote` fitting method using the `R band` image from MUSE data for the galaxy CGCG 012-116 and from DECaLS<sup>4</sup> data for the rest of the galaxies in order to get better results than with MUSE data cubes. In these images we mask other emitting sources such as other galaxies or stars in order to isolate the light coming from the object of interest and obtain good fits. From those fits we can then calculate the ellipticity,  $e$ , which is related to the inclination as  $i = \arccos(1 - e)$ , and the position angle at each radius.

As an example, in Fig. 11 we show the parameters as a function of the distance from the center of CGCG 012-116.

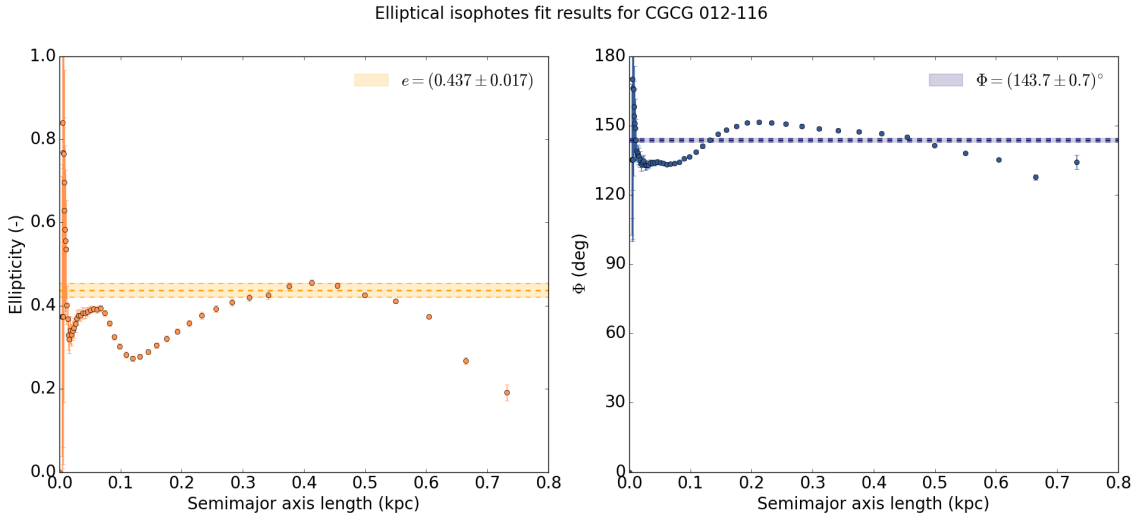


**Figure 11: Parameters ( $e$ ,  $\Phi$ ) of CGCG 012-116 obtained from isophote fittings.** Besides the ellipticity and the position angle of each isophote, we also show the mean value of each parameter for this galaxy using a dotted together with its uncertainty (coloured area).

In the case of the position angle, we had to perform some additional calculations before providing these values as input parameters for <sup>3D</sup>BAROLO taking into account two facts. First, the isophote fitting does not consider if the angle calculated is pointing to the approaching or receding half of the galaxy. Second, the algorithm calculates this angle from the positive side of X-axis but the data cubes we use have the North (N) direction aligned with the positive side of Y-axis and it is this N direction the reference one for the measurement of the PA in <sup>3D</sup>BAROLO. This means we have to apply two corrections: firstly, we must subtract  $90^\circ$  from the PA so it is calculated from the N direction; secondly, in the case where the PA is pointing to the approaching side of the galaxy, we must add  $180^\circ$  to it. In the case of CGCG 012-116, we obtain  $\Phi = (143.7 \pm 0.7)^\circ$ ; because this angle is for the approaching side of the galaxy, the corrected position angle will be  $\Phi^{correc.} = \Phi - 90^\circ + 180^\circ = (233.7 \pm 0.7)^\circ$ .

In Tab. 3 we show the mean parameters obtained from this analysis and that we use for the execution of <sup>3D</sup>BAROLO. An interesting observation is that CGCG 067-014 presents the greatest uncertainties: this galaxy has a very small ellipticity, which leads

<sup>4</sup>DECaLS (for DECam Legacy Survey) is a survey consisting of images by DECam (Dark Energy Camera) of the Víctor M. Blanco Telescope of a survey field selected from SDSS surveys. It includes observations for the purpose and data from other surveys by the same instrument. The aim has been to process the data to identify galaxies and their halos and to publicly release the resulting data (Blum et al., 2016).

us to assume that it is close to be face-on (Fig. 7), so the kinematical information we derive from its spectrum might be imprecise and future results will have to be carefully analysed. We also add in the last column of the table the recession velocities calculated previously.

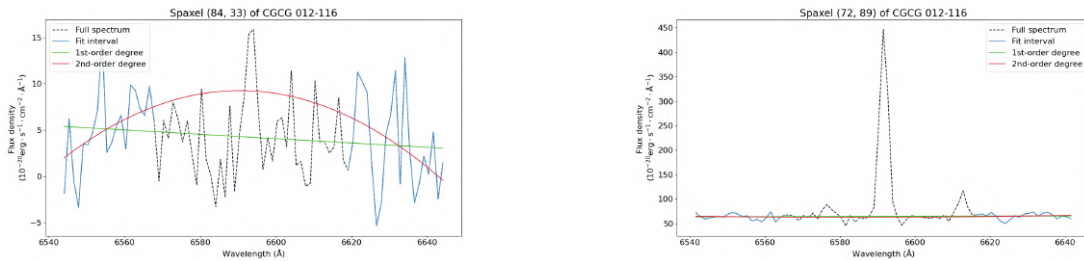
**Table 3: Geometrical parameters and recession velocities of the five galaxies.** The inclination has been calculated from the ellipticity and the position angle is corrected in order to be pointing to the receding half of the galaxy from the North direction. For each value we also estimate an uncertainty from the standard deviation of the data used in order to calculate the mean value.

Galaxy	Ellipticity	Inclination ( $^{\circ}$ )	Corrected position angle ( $^{\circ}$ )	$V_{rec}$ ( $km \cdot s^{-1}$ )
CGCG 067-014	$0.13 \pm 0.10$	$30 \pm 10$	$160 \pm 6$	1551.4
UGC 10023	$0.445 \pm 0.020$	$56.3 \pm 1.3$	$88.0 \pm 0.7$	$1371 \pm 7$
KUG 1201+220	$0.511 \pm 0.003$	$60.77 \pm 0.21$	$46.3 \pm 0.9$	$6409 \pm 3$
SDSS J164711.10+210527.0	$0.74 \pm 0.06$	$75 \pm 4$	$175 \pm 3$	$2626.8 \pm 2.1$
CGCG 012-116	$0.437 \pm 0.017$	$55.7 \pm 1.2$	$233.7 \pm 0.7$	$1276.2 \pm 1.1$

## 5.5 Continuum subtraction

Finally, the last step in order to use  $^3D$ BAROLO is to reduce the spectral range to a small interval around the  $H\alpha$  line and isolate the gas emission by fitting and subtracting the stellar continuum (because  $^3D$ BAROLO only uses emission lines for the fits). In order to do both tasks, we must fit the stellar continuum and then subtract it to the spectrum.

To crop the spectrum we use an interval of  $\pm 50 \text{ \AA}$  around the  $H\alpha$  emission line. In order to isolate the continuum emission and avoid the spectral lines (of  $H\alpha$  but also the two [NII] lines) we mask the values of the flux in an interval of  $\pm 25 \text{ \AA}$  around the  $H\alpha$  emission line to perform the fit. This combination was decided after probing with windows of  $\pm 50$  and  $\pm 100 \text{ \AA}$  and masked values in ranges of  $\pm 20$ ,  $\pm 25$  and  $\pm 30 \text{ \AA}$  around the  $H\alpha$  line. Finally, we fit the stellar continuum using a first-order polynomial function. We made a previous test for each galaxy comparing the results for a sample of spaxels using first and second-order polynomials and we saw that the second-order polynomial's fit was not as good as the first-order polynomial's. In Fig. 12 we show the results for CGCG 012-116 for different spaxels in the case of a global window of  $\pm 50 \text{ \AA}$  and masked values in a range of  $\pm 25 \text{ \AA}$ , both centered around the  $H\alpha$  emission line.



(a) Fits of the spaxel (84, 33).

(b) Fits of the spaxel (72, 89).

**Figure 12: Examples of test fittings of the stellar continuum for CGCG 012-116 in the case of a global window of  $\pm 50 \text{ \AA}$  and masked values in a range of  $\pm 25 \text{ \AA}$ .** As we can see in the case of spaxel (84, 33), for example, the fit of the polynomial with only one degree is good enough and gives better results than the 2-degrees fit, that tends to bend in the masked zone. Spaxel (72, 89) also shows that these ranges are correct, giving enough data to make good fits and hiding just enough values so the three emission lines ( $H\alpha$  and [NII]) stay out of the fit.

Now that we have established the best parameters for the fit of the stellar continuum, we proceed to apply them over the spectrum of each spaxel, for which the spectral range has been reduced around the  $H\alpha$  line restricting ourselves to the same 50 Å-window than for the fits. Every time a fit is made, the continuum is described as a mathematical function, allowing us then to subtract this mathematical function to all the cropped spectrum. It is important to understand that this process does not affect the intrinsic shape of the spectrum, which means that the ratios of intensity of each spectral channel stay the same, and even the noise level remains unaltered. An example of the process is visible in Fig. 13.

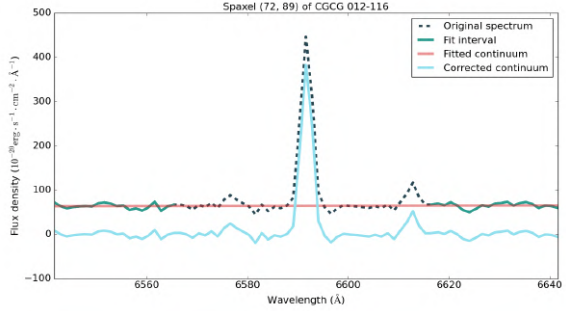


**Figure 13:** Example of the process of continuum subtraction with the spaxel (72, 89) of CGCG 012-116. We represent the spectrum before the fit in dashed-green line and the one corrected in blue. The shape of the spectrum suffers no modification, but we can see that the mean value of the stellar continuum is now fixed at a null flux density.

## 6 Results and discussion

In this section we show the results obtained using <sup>3D</sup>BAROLO on the kinematics of the galaxies, and the subsequent analyses made in order to determine their origins. We first discuss the rotation that takes place within the galaxies based on their rotation curves. Then we derive the 2D residual maps by subtracting the rotational model obtained with <sup>3D</sup>BAROLO to the observed velocity maps and describe the resulting non-circular motions. Finally, we analyse the so-called BPT diagram for some galaxies in order to determine the origin of their non-circular motions.

### 6.1 Rotation curves

Now that all the parameters needed for the fits of the 3D tilted-ring models are calculated (see § 5.4), we can apply <sup>3D</sup>BAROLO on our data. We use the data derived in § 5.5 and fix the parameters  $V_{rec}$ ,  $\Phi$ ,  $i$  and  $(x_0, y_0)$  using the values shown previously in Fig. 8 and Tab. 3.

<sup>3D</sup>BAROLO also needs some additional parameters: the **rotation velocity** ( $V_{rot}$ ), the **dispersion velocity** of the gas ( $\sigma_{gas}$ ), the **radial velocity** ( $V_{rad}$ ) and the width of the galaxy disk ( $z_0$ ). These parameters are chosen prior to the execution, so we can maximize the convergence of the results for each galaxy and get the best rotation models. The initial values of  $V_{rot}$  and  $V_{disp}$  were estimated using the program QFitsView<sup>5</sup> by calculating the 2D velocity maps. Because the objective is to fit only rotational motions of the gas (and its dispersion) and let non-rotational motion as residuals of this fit, we do not include radial motions in the model and fix the value of  $V_{rad} = 0 \text{ km} \cdot \text{s}^{-1}$ ; and we assume  $z_0 = 1''$  (infinitely thin disk approximation).

<sup>3D</sup>BAROLO uses emission lines in order to obtain the rotation curves. We initially set the software to detect three emission lines: the  $H\alpha$  line, at 6562.79 Å and the two

<sup>5</sup>Information about the software can be found on <https://www.mpe.mpg.de/~ott/QFitsView/>.

forbidden lines of [NII] at 6583.45 Å and 6548.08 Å. After a fruitful discussion with the creator of the code (Dr. Enrico Di Teodoro, JHU/STScI), we restricted the fit to the use of only the  $H\alpha$  line. The reason is that in general the performance of  $3^{\text{D}}$ BAROLO is better using just one emission line. We therefore select  $H\alpha$  since generally it is the most intense line and the one presenting the best coverage across the galaxy disk.

The goal with  $3^{\text{D}}$ BAROLO is to fit both the rotational velocity and the dispersion velocity of the gas, making sure that our model properly describes the rotation of the galaxy. Once the rotation is fully modelled, we can then investigate the residual motions extracted by subtracting the model to the data. Let's first study the rotation in this section.

In Fig. 14, we show the rotation curves derived using  $3^{\text{D}}$ BAROLO.

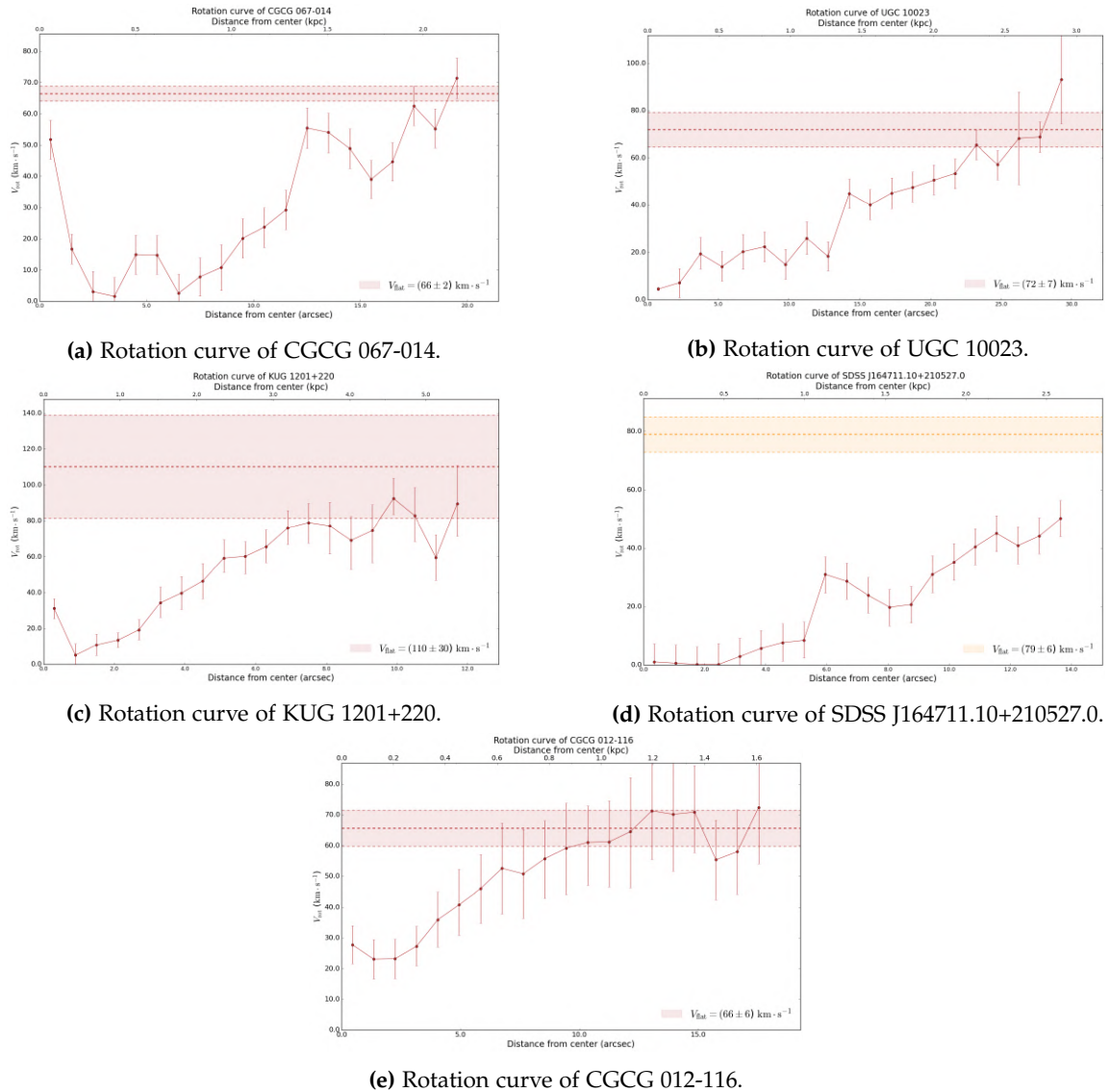
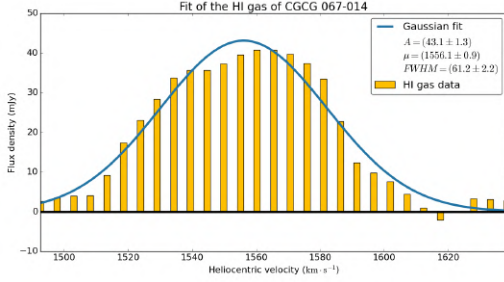
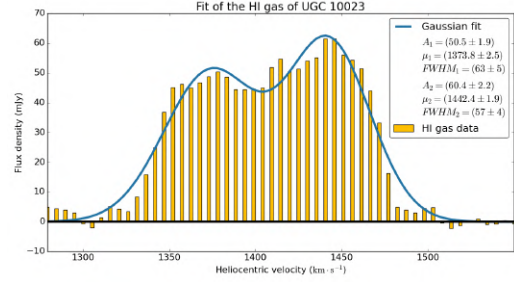


**Figure 14: Rotation curves of the five galaxies.** We represent both the data derived from  $3^{\text{D}}$ BAROLO and the value of  $V_{flat}$  in red, calculated using data from the Arecibo Legacy Fast ALFA Survey (Haynes et al., 2018) for all the galaxies except SDSS J164711.10+210527.0, whose data come from the HI Parkes All Sky Survey (Barnes et al., 2001).

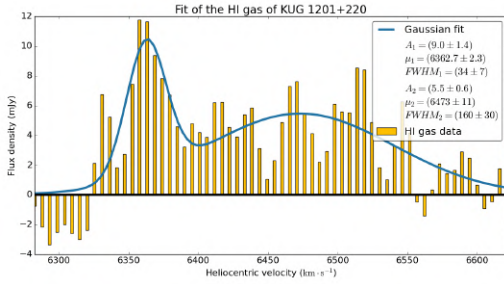
In Fig. 14 we also show as a dotted line the velocity at which the rotation curves flatten ( $V_{flat}$ ) together with its uncertainty (coloured area). In most cases, the observed maximum rotation velocity coincides with the value of  $V_{flat}$  calculated using atomic HI gas. However, there is an exception: SDSS J164711.10+210527.0 is a galaxy in an advanced stage of interaction and it might be the case that the data from HIPASS used to determine  $V_{flat}$  include the motions of its companion (Privon et al., 2017), making  $V_{flat}$  greater than its actual value for this galaxy; this is why we plot its  $V_{flat}$  in yellow. The procedure to obtain these values is explained in § 2.5 and the fits used for the estimation of  $V_{flat}$  are shown together with the values of the parameters in Fig. 15.



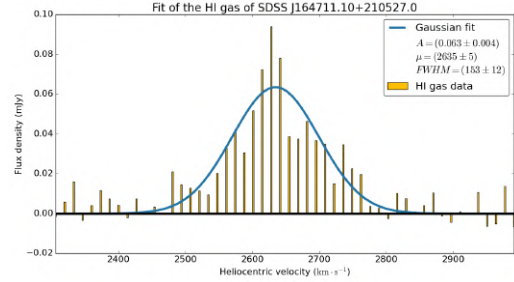
(a) Gaussian fit of the HI gas of CGCG 067-014.



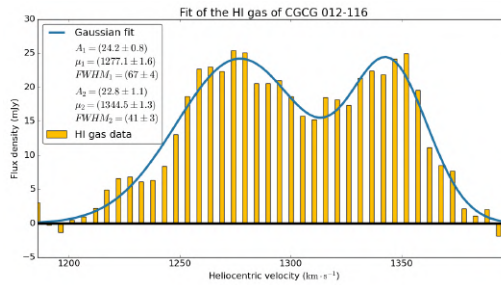
(b) Gaussian fit of the HI gas of UGC 10023.



(c) Gaussian fit of the HI gas of KUG 1201+220.



(d) Gaussian fit of the HI gas of SDSS J164711.10+210527.0.



(e) Gaussian fit of the HI gas of CGCG 012-116.

**Figure 15: One-peak and two-peak gaussian fits of the five galaxies used for the estimation of  $V_{flat}$ .** In the case where two peaks were visible, we applied a double gaussian fit but when only one is distinguishable we only applied a simple gaussian fit and estimated  $V_{flat}$  using the FWHM, as explained in § 2.5.

An interesting analysis to make is the comparison between  $R_{max}$  and  $R_{90}$ . The first parameter represents the distance from the center to the position at which maximum velocity is reached in the rotation curve. The latter corresponds to the radius containing 90% of the Petrosian flux in the R band<sup>6</sup> and it is related to  $D_{25}$ , the major diameter of the isophote at a surface brightness level of  $\mu_B = 25 \text{ mag} \cdot \text{arcsec}^{-2}$ , as  $D_{25} = 3 \cdot R_{90}$  (Duarte-Puertas et al., in prep.). Here we use values of  $R_{90}$  obtained from the SDSS Data Release 16 (Ahumada et al., 2020) and both  $R_{max}$  and  $R_{90}$  but also the ratio  $R_{max}/R_{90}$  are shown in Tab. 4. With these results we can confirm <sup>3D</sup>BAROLO fitted the rotation of the galaxies for almost all the visible disk since the ratio is always greater than 0.8, which is a great coverage. Thus, we have shown that in most cases the rotation curve reaches  $V_{flat}$ , supporting the good coverage of the data across the galaxies' disks. In the case of SDSS J164711.10+210527.0, the abnormally low value of  $R_{90}$  make us think that the data used for its estimation are probably erroneous due to the interacting galaxy nearby, as it was for  $V_{flat}$ .

**Table 4: Comparison table between  $R_{max}$  and  $R_{90}$ .**

Galaxy	$R_{90}$ (arcsec)	$R_{max}$ (arcsec)	$R_{max}/R_{90}$
CGCG 067-014	19.30	$19.5 \pm 1.0$	$1.01 \pm 0.05$
UGC 10023	23.20	$29.3 \pm 1.0$	$1.26 \pm 0.04$
KUG 1201+220	12.25	$9.9 \pm 1.0$	$0.81 \pm 0.08$
SDSS J164711.10+210527.0	1.34	$13.7 \pm 1.0$	$10.2 \pm 0.7$
CGCG 012-116	12.17	$17.6 \pm 1.0$	$1.45 \pm 0.08$

## 6.2 2D residual velocity maps

The 2D maps provided by <sup>3D</sup>BAROLO are shown in this section (Figs. 16-20). For each galaxy we represent the observed 2D velocity map calculated with the  $H\alpha$  emission lines (data), the rotation model fitted by the software using the [tilted-ring model](#) and the residual velocity map, obtained by subtracting the model to the data. On the first two maps we show with green contours the areas in the model where  $V_{los} = 0 \text{ km} \cdot \text{s}^{-1}$ ; in the residual velocity map we represent with black contours the regions of most intense  $H\alpha$  integrated flux, in order to compare the regions with most ionized gas with the regions where non-circular motions appear.

In the case of CGCG 064-014 (Fig. 16), the rotation model is correctly fitting the data despite the low inclination of the disk. In the residual velocity map we clearly see regions with very high non-circular motions, greater than  $50 \text{ km} \cdot \text{s}^{-1}$ , especially in the right side of the galaxy where a lot of ionized gas concentrates.

<sup>6</sup>The Petrosian flux is defined as the flux contained within twice the Petrosian radius, the circular radius at which the local surface brightness  $\mu(r)$  is equal to 20 per cent of the enclosed mean surface brightness  $\mu(< r)$  (Blanton et al., 2001). This parameter is normally used as an estimation of the size of the galaxy.

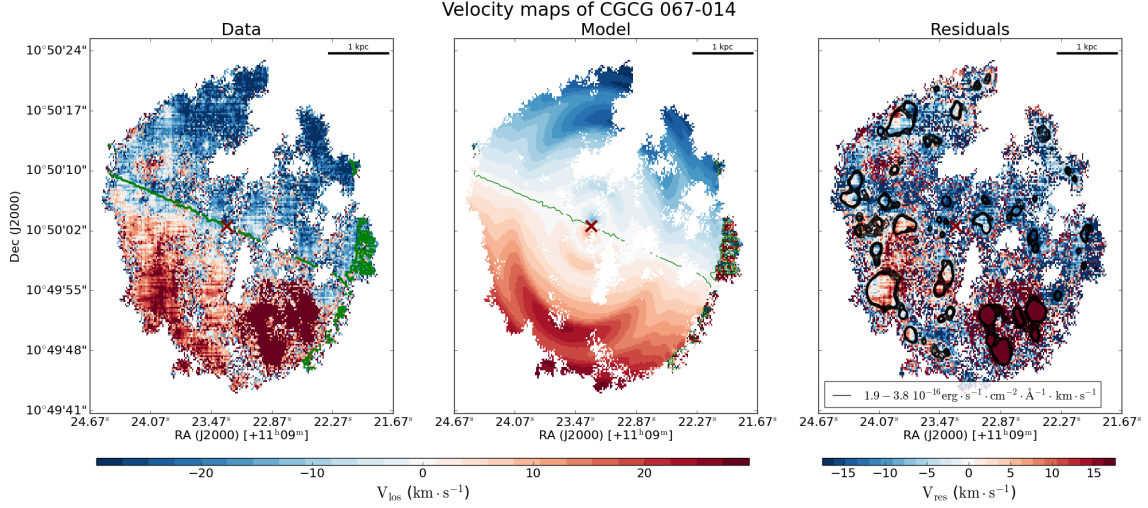


Figure 16: Velocity maps of CGCG 067-014.

UGC 10023 (Fig. 17) is an irregular type galaxy (de Vaucouleurs et al., 1991), which explains the shape of its disk. However, we clearly see the rotation in the model derived by the software with the receding and approaching sides and we can also observe how the velocity grows with the distance, reaching  $90 \text{ km} \cdot \text{s}^{-1}$  in its outer radii. However, the residual velocities do not seem to show a clear pattern: we observe stochastic motions reaching values between 15 and  $20 \text{ km} \cdot \text{s}^{-1}$ . Besides, the contours of flux intensity do not show any pattern neither nor seem related to any specific region of the 2D velocity map.

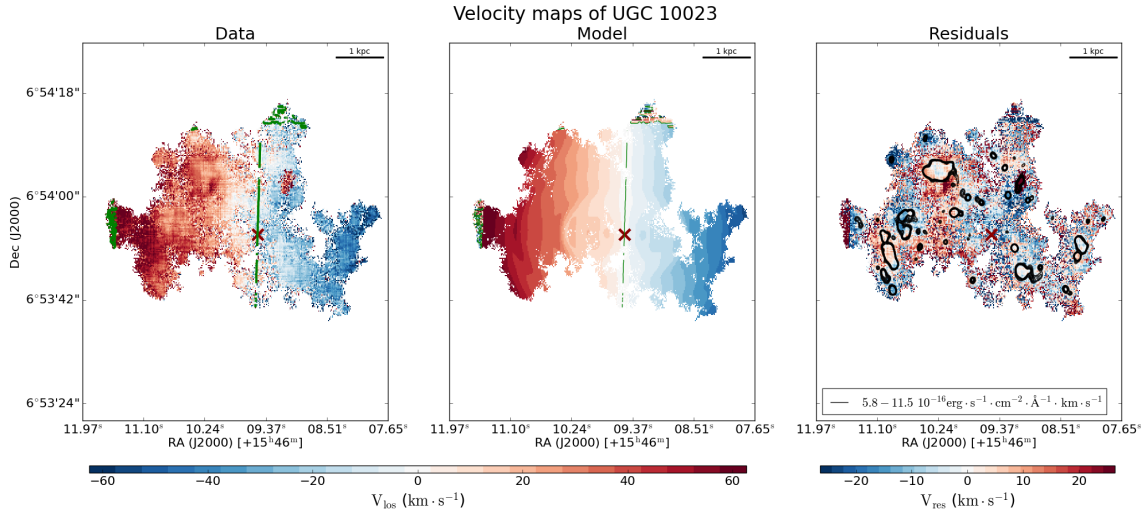


Figure 17: Velocity maps of UGC 10023.

KUG 1201+220 (Fig. 18) shows a clear rotation in its model map, with velocities in our line of sight reaching  $80 \text{ km} \cdot \text{s}^{-1}$ . The model we see here is typical of a barred galaxy, with velocities constant in regions parallel to the minor axis (see Fig. 2b for a more theoretical case), and the orientation of both the bar and the disk semi-major axes coincide. Its non-rotational velocities (right panel) seem to recess on the left side of the galaxy and approach on the right side of the map; this phenomenon might be caused by a warp in the outer regions of the galaxy, which is a distortion of the disk. Even if we still do not understand fully the origin of warps, in this case it might be caused by the bar, satellite galaxies or in general any instability in the gravitational potential (Kuijken

and Garcia-Ruiz, 2001). Here the flux distribution seems to follow the main axis of the disk, which can be explained by the presence of a higher density of ionized gas in the bar, maybe due to internal dynamical processes like star formation.

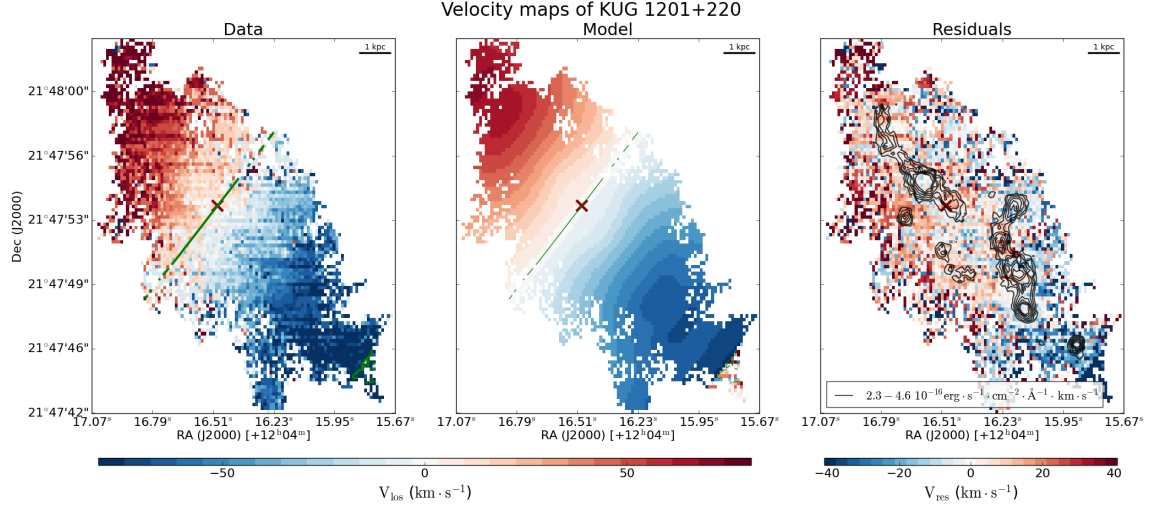


Figure 18: Velocity maps of KUG 1201+220.

SDSS J164711.10+210527.0 (Fig. 19) is strongly interacting with another galaxy (Privon et al., 2017), hampering the modelling of the velocity field and the rotation curve. In order to isolate the galaxy from the companion, we ran <sup>3D</sup>BAROLO using different sets of masks, but the velocity maps were all very similar regardless of the mask used. Despite this interaction, we see a clear rotation in its model velocity map, with values reaching almost  $50 \text{ km} \cdot \text{s}^{-1}$  in the outer regions. Its residual velocity map shows a random distribution of non-circular motions, but with more recessing material in the central regions while more external ones harbor blueshifted velocities, especially on the East and West sides. The N-E region is dominated by recessing gas. This pattern may be caused by global motions outside the disk, like a warp, maybe induced by the interaction with the companion galaxy. Flux distribution show a more stochastic distribution, with contours of same intensity around both recessing and approaching regions.

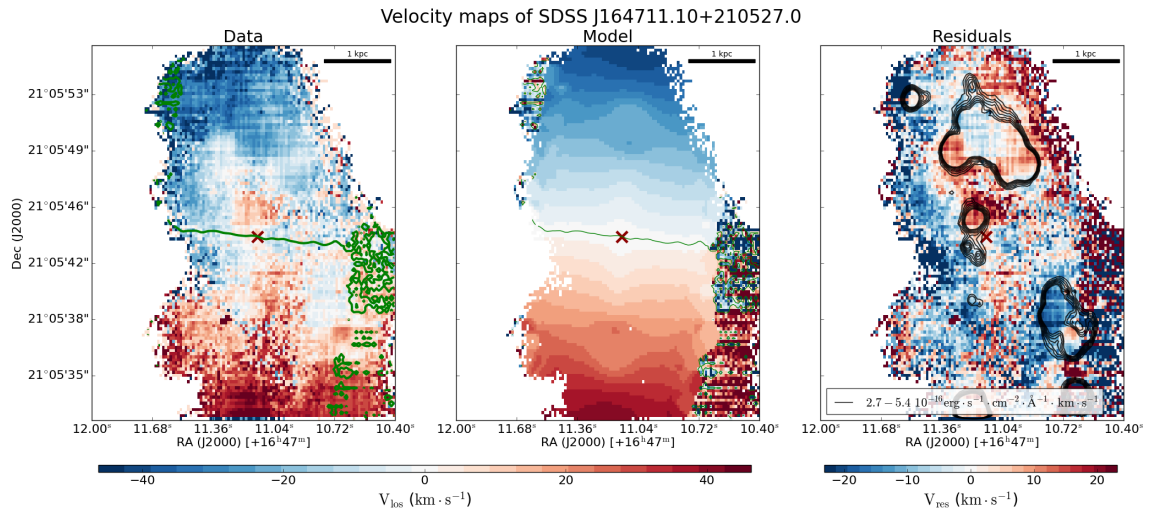
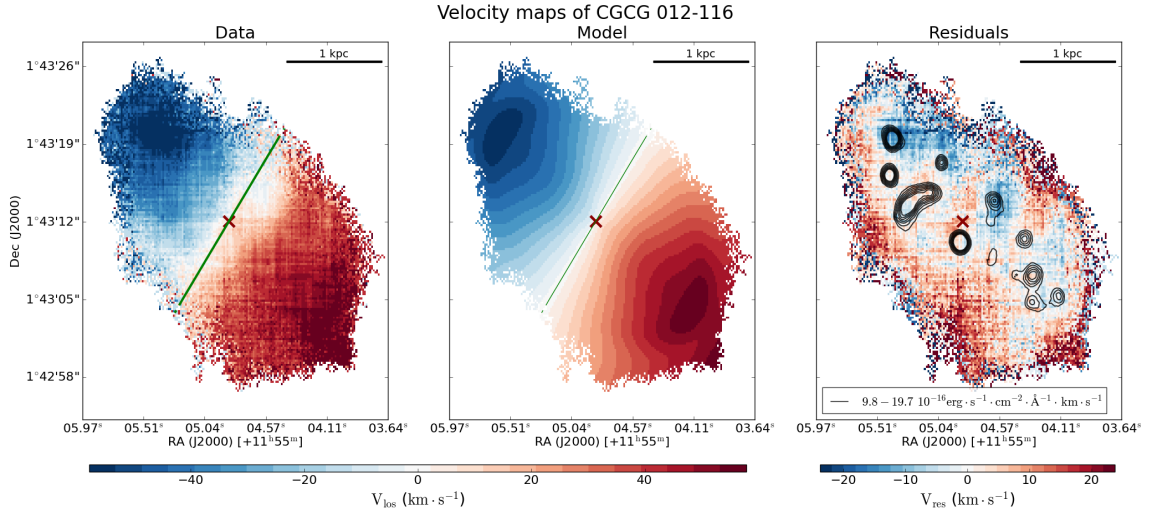


Figure 19: Velocity maps of SDSS J164711.10+210527.0.

Finally, CGCG 012-116 (Fig. 20) also displays a model with a very clear rotation, with velocities in our line of sight of  $60\text{--}70 \text{ km} \cdot \text{s}^{-1}$  in the outer regions of the disk. Besides, an interesting observation is that the regions with negative residual velocities appear to be hosting gas highly ionized, demonstrating a relation between the residual motions and the star formation regions further discussed in the following subsection.



**Figure 20:** Velocity maps of CGCG 012-116.

About the high velocities found at low radii for CGCG 067-014 and CGCG 012-116 in their rotation curves (see Figs. 14a and 14e), we now see that their velocity maps clearly show that the central regions have velocities near  $0 \text{ km} \cdot \text{s}^{-1}$ , as expected (see § 2.4). The discrepancy between the central values for the rotation curve and the velocity maps need to be further investigated in future work and seems to be related to the rotation curves delivered by <sup>3D</sup>BAROLO as the 2D maps give the right rotational velocities in both the internal and the external parts.

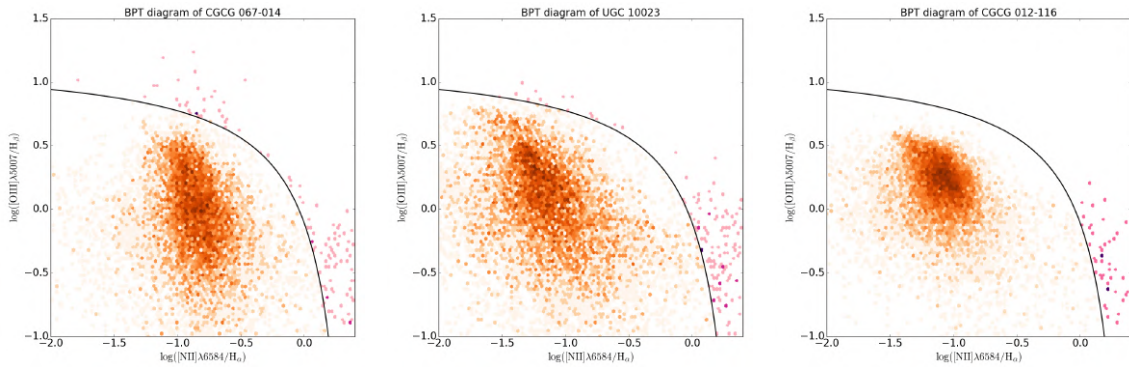
It is relevant to mention that the residual motions we calculate are reaching their maximum values at about one third to one half the maximum velocities of the data, while KUG 1201+220 is having non-circular motions much higher, with an intensity more than two third the maximum of its data velocities. As we can see, non-circular motions are not negligible, even when they seem to follow a stochastic distribution, and in the case of a central structure like a strong bar, they may become very relevant.

### 6.3 Complementary analysis

After using <sup>3D</sup>BAROLO for the characterization of the non-rotational motions, we have seen that in several cases (CGCG 067-014, UGC 10023 and CGCG 012-116) these motions are stochastic and linked to regions where the presence of ionised gas is higher. In order to determine the origin of these motions and whether they are related to star formation or not, we analyze their BPT diagrams. A BPT diagram has for the first time been shown in an article of Baldwin, Philips and Terlevich (Baldwin et al., 1981): the representation of  $\log ([OIII]/H\beta)$  as a function of  $\log ([NII]/H\alpha)$  gives us information about the ionization processes of each zone of the galaxy: star-formation regions (SFR) or non star-formation regions (NSFR). This second category includes active galactic nuclei (AGN) and low-ionization nuclear emission-line regions (LINERs). The LINER emission is found in a large percentage of galaxies and its origin is associated to several processes, such as shock excitation (Heckman, 1980), photoionization (Ho et al., 1993; Veilleux et al., 1995; Terlevich and Melnick, 1985) or ionization by old population stars (Cid Fernandes et al., 2010).

In order to create BPT diagrams for each galaxy, we used data obtained from applying Pipe3D (Sánchez et al., 2016) to our data cubes, which is a program that fits the emission of the gas and stellar populations in the spectra of the spaxels and, as a result, get the intensity of each emission line. We used values and uncertainties of each emission line so we could apply a criterion to determine if a spaxel had a significant intensity at a specific line or if it is at the level of the noise: because we use four lines ( $H\alpha$ ,  $H\beta$ ,  $[NII]\lambda 6584\text{\AA}$  and  $[OIII]\lambda 5007\text{\AA}$ ) and the weakest one is the  $[OIII]$  line, we decided to not consider spaxels with a value of  $[OIII]\lambda 5007\text{\AA}$ 's intensity smaller than its own uncertainty.

In Fig. 21 we show the BPT diagrams of CGCG 064-014, UGC 10023 and CGCG 012-116, which are the galaxies where stochastic residual motions seem related with regions of high  $H\alpha$  flux intensity. We discovered that most of the spaxels were actually categorized as star-formation regions. This suggests that the regions presenting higher non-circular motions are indeed associated with star formation processes. They might be regions with expanding shells of ionized gas, which would mean that star formation processes are inducing local internal non-circular motions within the gas of the galaxies.



(a) BPT diagram of CGCG 067-014. (b) BPT diagram of UGC 10023. (c) BPT diagram of CGCG 012-116.

**Figure 21: BPT diagrams of CGCG 064-014, UGC 10023 and CGCG 012-116.** These BPT diagrams show, in yellow, spaxels of the data cubes that corresponds to star-formation regions (SFR) and, in pink/purple non star-formation regions (NSFR), using the model described in Kewley et al. (2001) (eq. 5). SFR are the clear majority for all the galaxies.

## 7 Conclusions and future work

We analysed the kinematics of five low-mass galaxies from the AMUSING++ survey using a state-of-the-art software named <sup>3D</sup>BAROLO. Firstly, we perform several analyses in order to derive the input parameters required by the code and then used the software to calculate and model the rotation of the galaxies.

All the galaxies of this study showed a rotation curve typical of more massive spiral galaxies, with increasing velocities in the central part of the disk that flatten in the external radii. This confirms the hypothesis that low-mass galaxy disks are indeed kinematically supported by rotation. Another remarkable result is that all the galaxies have rotation curves that reach the flattening value derived from HI data<sup>7</sup>, so the data used here may be used in the future for further analysis, especially for dark matter studies.

We confirmed that one of the galaxies, CGCG 067-014, has a very low inclination of  $(30 \pm 10)^\circ$ , however <sup>3D</sup>BAROLO managed to make a correct analysis of its rotation. Another galaxy in the sample, KUG 1201+220, shows a rotation curve compatible with that of a rigid body, implying the presence of a bar in its central region, which might have induced some of the observed non-circular motions. In addition, despite the strong interaction SDSS J164711.10+210527.0 suffers with its companion, its disk is still dominated by the rotation.

After modelling the rotation curves, we were able to analyze the residual velocities of the galaxies and investigate the presence of non-circular motions. In the case of KUG 1201+220 and SDSS J164711.10+210527.0, their residual velocity maps are compatible with the presence of a warp (distortion in the disk), maybe induced by external gravitational torques.

On a more local scale, the residual velocity maps of several galaxies (CGCG 067-014, UGC 10023 and CGCG 012-116) show us non-circular motions stochastically distributed over the disks and spatially coincident with regions of ionized gas. Analysing the BPT diagram for these galaxies we observe that these regions are associated with star formation, suggesting that some of these non-circular motions might be induced by star formation processes.

However, it is important not to forget that more analysis need to be done in order to better understand the processes that induce the non-circular motions observed in low-mass galaxies. An example, as we stated briefly in § 2.7, is the need to study the dark matter component of the halo and its effect on the gravitational potential that then induce non-rotational motions.

Finally, we can conclude for all the galaxies that, as stated in [Oman et al. \(2019\)](#); [Marasco et al. \(2018\)](#), it is clear that non-rotational motions are not negligible in relation to rotational ones, especially in the case of a barred galaxy.

In the future, studies with HI gas and about dark matter and its effect on the gravitational potential may clarify the situation and determine if these non-circular motions are whether or not originated by some internal processes.

---

<sup>7</sup>SDSS J164711.10+210527.0's rotation curve might not be reaching  $V_{flat}$  because, as it is a galaxy in an advanced stage of interaction, the data from HIPASS used to determine  $V_{flat}$  include the motions of its companion and make  $V_{flat}$  higher than its actual value.

## References

- R. Ahumada et al. [The 16th Data Release of the Sloan Digital Sky Surveys: First Release from the APOGEE-2 Southern Survey and Full Release of eBOSS Spectra](#). *The Astrophysical Journal Supplement Series*, 249(1):3, July 2020. doi: 10.3847/1538-4365/ab929e. 24
- R. Bacon et al. [The MUSE second-generation VLT instrument](#). In *Ground-based and Airborne Instrumentation for Astronomy III*, volume 7735 of *Society of Photo-Optical Instrumentation Engineers (SPIE) Conference Series*, page 773508, July 2010. doi: 10.1117/12.856027. 13
- J. A. Baldwin, M. M. Phillips, and R. Terlevich. [Classification parameters for the emission-line spectra of extragalactic objects](#). , 93:5–19, February 1981. doi: 10.1086/130766. 28
- D. G. Barnes et al. [The HI Parkes All Sky Survey: southern observations, calibration and robust imaging](#). *Monthly Notices of the Royal Astronomical Society*, 322(3):486–498, April 2001. doi: 10.1046/j.1365-8711.2001.04102.x. 22
- K. G. Begeman. [HI rotation curves of spiral galaxies](#). PhD thesis, University of Groningen, Kapteyn Astronomical Institute, December 1987. 12
- M. R. Blanton et al. [The Luminosity Function of Galaxies in SDSS Commissioning Data](#). *The Astronomical Journal*, 121(5):2358–2380, May 2001. doi: 10.1086/320405. 24
- R. D. Blum, K. Burleigh, A. Dey, D. J. Schlegel, A. M. Meisner, M. Levi, A. D. Myers, D. Lang, J. Moustakas, A. Patej, F. Valdes, J.-P. Kneib, S. Huanyuan, B. Nord, K. A. Olsen, T. Delubac, A. Saha, D. James, A. R. Walker, and DECaLS Team. [“The DECam Legacy Survey”](#). In *American Astronomical Society Meeting Abstracts #228*, volume 228 of *American Astronomical Society Meeting Abstracts*, page 317.01, June 2016. 19
- F. Bonnarel, P. Fernique, O. Bienaymé, D. Egret, F. Genova, M. Louys, F. Ochsenbein, M. Wenger, and J. G. Bartlett. [The ALADIN interactive sky atlas. A reference tool for identification of astronomical sources](#). *Astronomy and Astrophysics, Supplement*, 143: 33–40, April 2000. doi: 10.1051/aas:2000331. 13
- R. Boomsma, T. A. Oosterloo, F. Fraternali, J. M. van der Hulst, and R. Sancisi. [HI holes and high-velocity clouds in the spiral galaxy NGC 6946](#). *Astronomy and Astrophysics*, 490(2):555–570, November 2008. doi: 10.1051/0004-6361:200810120. 9
- A. Bosma. [The distribution and kinematics of neutral hydrogen in spiral galaxies of various morphological types](#). PhD thesis, University of Groningen, Netherlands, March 1978. 10
- K. C. Chambers et al. [The Pan-STARRS1 Surveys](#). *arXiv e-prints*, art. arXiv:1612.05560, December 2016. 13
- R. Cid Fernandes, G. Stasińska, M. S. Schlickmann, A. Mateus, N. Vale Asari, W. Schoenell, and L. Sodré. [Alternative diagnostic diagrams and the ‘forgotten’ population of weak line galaxies in the SDSS](#). *Monthly Notices of the Royal Astronomical Society*, 403(2):1036–1053, April 2010. doi: 10.1111/j.1365-2966.2009.16185.x. 28
- G. de Vaucouleurs, A. de Vaucouleurs, Jr. Corwin, H. G., R. J. Buta, G. Paturel, and P. Fouque. [Third Reference Catalogue of Bright Galaxies](#). 1991. 25
- E. M. Di Teodoro and J. E. G. Peek. [Radial Motions and Radial Gas Flows in Local Spiral Galaxies](#). *The Astrophysical Journal*, 923(2):220, December 2021. doi: 10.3847/1538-4357/ac2cbd. 11

- S. Duarte-Puertas et al. in prep. 24
- K. M. Ferrière. [The interstellar environment of our galaxy](#). *Reviews of Modern Physics*, 73(4):1031–1066, October 2001. doi: 10.1103/RevModPhys.73.1031. 9
- M. Franx, J. H. van Gorkom, and T. de Zeeuw. [Evidence for Axisymmetric Halos: The Case of IC 2006](#). *The Astrophysical Journal*, 436:642, December 1994a. doi: 10.1086/174939. 11
- M. Franx, J. H. van Gorkom, and T. de Zeeuw. [Evidence for Axisymmetric Halos: The Case of IC 2006](#). *The Astrophysical Journal*, 436:642, December 1994b. doi: 10.1086/174939. 6
- K. C. Freeman. [On the Disks of Spiral and S0 Galaxies](#). *The Astrophysical Journal*, 160:811, June 1970. doi: 10.1086/150474. 7
- M. P. Haynes et al. [The Arecibo Legacy Fast ALFA Survey: The ALFALFA Extragalactic H I Source Catalog](#). *The Astrophysical Journal*, 861(1):49, July 2018. doi: 10.3847/1538-4357/aac956. 22
- T. M. Heckman. [An Optical and Radio Survey of the Nuclei of Bright Galaxies - Activity in the Normal Galactic Nuclei](#). *Astronomy and Astrophysics*, 87:152, July 1980. 28
- L. C. Ho, A. V. Filippenko, and W. L. W. Sargent. [A Reevaluation of the Excitation Mechanism of LINERs](#). *The Astrophysical Journal*, 417:63, November 1993. doi: 10.1086/173291. 28
- R. I. Jedrzejewski. [CCD surface photometry of elliptical galaxies - I. Observations, reduction and results](#). *Monthly Notices of the Royal Astronomical Society*, 226:747–768, June 1987. doi: 10.1093/mnras/226.4.747. 18
- L. J. Kewley, M. A. Dopita, R. S. Sutherland, C. A. Heisler, and J. Trevena. [Theoretical Modeling of Starburst Galaxies](#). *The Astrophysical Journal*, 556(1):121–140, July 2001. doi: 10.1086/321545. 28
- K. Kuijken and I. Garcia-Ruiz. [Galactic Disk Warps](#). In José G. Funes and Enrico Maria Corsini, editors, *Galaxy Disks and Disk Galaxies*, volume 230 of *Astronomical Society of the Pacific Conference Series*, pages 401–408, January 2001. 25
- C López-Cobá, S. F. Sánchez, J. P. Anderson, I. Cruz-González, L. Galbany, T. Ruiz-Lara, J. K. Barrera-Ballesteros, J. L. Prieto, and H. Kuncarayakti. [The AMUSING++ Nearby Galaxy Compilation. I. Full Sample Characterization and Galactic-scale Outflow Selection](#). *Astronomical Journal*, 159(4):167, April 2020. doi: 10.3847/1538-3881/ab7848. 13
- A. Marasco, K. A. Oman, J. F. Navarro, C. S. Frenk, and T. Oosterloo. [Bars in dark-matter-dominated dwarf galaxy discs](#). *Monthly Notices of the Royal Astronomical Society*, 476(2): 2168–2176, May 2018. doi: 10.1093/mnras/sty354. 11, 29
- K. A. Oman, A. Marasco, J. F. Navarro, C. S. Frenk, J. Schaye, and A. Benítez-Llambay. [Non-circular motions and the diversity of dwarf galaxy rotation curves](#). *Monthly Notices of the Royal Astronomical Society*, 482(1):821–847, January 2019. doi: 10.1093/mnras/sty2687. 11, 29
- G. C. Privon, S. Stierwalt, D. R. Patton, G. Besla, S. Pearson, M. Putman, K. E. Johnson, N. Kallivayalil, S. Liss, and TiNy Titans. [A Widespread, Clumpy Starburst in the Isolated Ongoing Dwarf Galaxy Merger dm1647+21](#). *The Astrophysical Journal*, 846(1): 74, September 2017. doi: 10.3847/1538-4357/aa8560. 14, 23, 26

- G. Rhee, O. Valenzuela, A. Klypin, J. Holtzman, and B. Moorthy. [The Rotation Curves of Dwarf Galaxies: A Problem for Cold Dark Matter?](#) *The Astrophysical Journal*, 617(2): 1059–1076, December 2004. doi: 10.1086/425565. 11
- D. H. Rogstad, I. A. Lockhart, and M. C. H. Wright. [Aperture-synthesis observations of H I in the galaxy M83.](#) *Astrophysical Journal*, 193:309–319, October 1974. doi: 10.1086/153164. 12
- V. C. Rubin, Jr. Ford, W. K., and N. Thonnard. [Rotational properties of 21 SC galaxies with a large range of luminosities and radii, from NGC 4605 \(R=4kpc\) to UGC 2885 \(R=122kpc\).](#) *The Astrophysical Journal*, 238:471–487, June 1980. doi: 10.1086/158003. 7
- R. Z. Sanchez. [Measuring mass: Non-circular motions of gas in disk galaxies and radial velocities of stars in a globular cluster.](#) PhD thesis, Rutgers University, New Jersey, November 2009. 11
- S. F. Sánchez, E. Pérez, P. Sánchez-Blázquez, J. J. González, F. F. Rosáles-Ortega, M. Cano-Díaz, C. López-Cobá, R. A. Marino, A. Gil de Paz, M. Mollá, A. R. López-Sánchez, Y. Ascasibar, and J. Barrera-Ballesteros. [Pipe3D, a pipeline to analyze Integral Field Spectroscopy Data: I. New fitting philosophy of FIT3D.](#) *Revista Mexicana de Astronomía y Astrofísica*, 52:21–53, April 2016. 28
- R. H. Sanders and S. S. McGaugh. [Modified Newtonian Dynamics as an Alternative to Dark Matter.](#) *Annual Review of Astronomy and Astrophysics*, 40:263–317, January 2002. doi: 10.1146/annurev.astro.40.060401.093923. 7
- R. H. M. Schoenmakers, M. Franx, and P. T. de Zeeuw. [Measuring non-axisymmetry in spiral galaxies.](#) *Monthly Notices of the Royal Astronomical Society*, 292(2):349–364, December 1997. doi: 10.1093/mnras/292.2.349. 11
- J. A. Sellwood and A. Kosowsky. [Does Dark Matter Exist?](#) In John E. Hibbard, Michael Rupen, and Jacqueline H. van Gorkom, editors, *Gas and Galaxy Evolution*, volume 240 of *Astronomical Society of the Pacific Conference Series*, page 311, January 2001. 7
- F. Shu. [The Physical Universe: An Introduction to Astronomy.](#) Series of books in astronomy. University Science Books, 1982. ISBN 0-935702-05-9. 7, 9
- K. Spekkens and J. A. Sellwood. [Modeling Noncircular Motions in Disk Galaxies: Application to NGC 2976.](#) *The Astrophysical Journal*, 664(1):204–214, July 2007. doi: 10.1086/518471. 11, 12
- E. M. Di Teodoro and F. Fraternali. [3DBAROLO: a new 3D algorithm to derive rotation curves of galaxies.](#) *Monthly Notices of the Royal Astronomical Society*, 451(3):3021–3033, 06 2015. ISSN 0035-8711. doi: 10.1093/mnras/stv1213. 11, 12
- R. Terlevich and J. Melnick. [Warmers : the missing link between Starburst and Seyfert galaxies.](#) *Monthly Notices of the Royal Astronomical Society*, 213:841–856, April 1985. doi: 10.1093/mnras/213.4.841. 28
- P. J. Teuben. [Velocity Fields of Disks in Triaxial Potentials.](#) In *Warped Disks and Inclined Rings around Galaxies*, page 40, January 1991. 11
- O. Valenzuela, G. Rhee, A. Klypin, F. Governato, G. Stinson, T. Quinn, and J. Wadsley. [Is There Evidence for Flat Cores in the Halos of Dwarf Galaxies? The Case of NGC 3109 and NGC 6822.](#) *The Astrophysical Journal*, 657(2):773–789, March 2007. doi: 10.1086/508674. 11
- R. P. van der Marel, G. Besla, T. J. Cox, S. T. Sohn, and J. Anderson. [The M31 Velocity](#)

- Vector.** III. Future Milky Way M31-M33 Orbital Evolution, Merging, and Fate of the Sun. *The Astrophysical Journal*, 753(1):9, July 2012. doi: 10.1088/0004-637X/753/1/9. 5
- S. Veilleux, D. C. Kim, D. B. Sanders, J. M. Mazzarella, and B. T. Soifer. **Optical Spectroscopy of Luminous Infrared Galaxies. II. Analysis of the Nuclear and Long-Slit Data.** *The Astrophysical Journals*, 98:171, May 1995. doi: 10.1086/192158. 28
- L. Verdes-Montenegro et al. **HI and galaxy evolution.** In *The Spanish Square Kilometre Array White Book*, pages 47–62. Red de Infraestructuras de Astronomía, June 2015. 9
- A. Wojnar, C. Sporea, and A. Borowiec. **A Simple Model for Explaining Galaxy Rotation Curves.** *Galaxies*, 6(3):70, July 2018. doi: 10.3390/galaxies6030070. 7, 8
- This research has made use of the NASA/IPAC Extragalactic Database (NED), which is operated by the Jet Propulsion Laboratory, California Institute of Technology, under contract with the National Aeronautics and Space Administration.

## Glossary

- dark matter** A hypothesis that proposes that an invisible mass makes up outer regions of the galaxies in order to explain the flat rotation curves observed without modifying dynamical laws. 7
- data cube** Also called “spectral data cube”, it is a three-dimensional array of data values, where the first two dimensions are spatial ones and the third one is a spectral dimension (here in wavelength). 12, 28
- dispersion velocity** Spread of velocities of stars or gas in a galaxy. 21
- Doppler effect** Change in frequency of a wave in relation to an observer who is moving relative to the wave source. 5, 6
- edge-on** Inclination of the galaxy whose rotation axis is perpendicular to the line of sight. 10, 15
- face-on** Inclination of the galaxy whose rotation axis is parallel to the line of sight. 15
- Hubble flow** It describes the motion of galaxies due solely to the expansion of the Universe. 6
- Hubble type** The Hubble sequence is a morphological classification scheme for galaxies invented by Edwin Hubble in 1926. It divides galaxies into elliptical galaxies, spiral galaxies, lenticular galaxies and irregular galaxies. 5
- isophote** Curve on a surface connecting points of equal luminosity. 18, 19
- MOND** Modified Newtonian dynamics (MOND) is a hypothesis that proposes a modification of the acceleration of Newton’s law of gravitation in order to explain the flat rotation curves observed without the need to bring new invisible mass. 7
- parsec** Unit of length used to measure large distances in astronomy. It is approximately equal to 3.26 light-years. 5
- R band** Photometric system’s red band, a typical example being centered round 658 nm with a full width at half maximum of 138 nm. 15, 16, 19

- radial velocity** Velocities measured in the radial axis of the disk of the galaxy. [21](#)
- recession velocity** Name given in astronomy to the speed at which an extragalactic object moves away from an observer, due to the expansion of the universe. [5, 7](#)
- redshift** Displacement of the spectrum of an astronomical object toward longer (red) wavelengths. It is attributed to the Doppler effect, a change in wavelength that results when a given source of waves (e.g., light or radio waves) and an observer are in motion with respect to each other. [6](#)
- rotation curve** Plot of the orbital speeds of visible stars or gas in that galaxy versus their radial distance from that galaxy's centre. [7, 8](#)
- rotation velocity** Velocity of star or gas in the angular direction caused by the gravitational potential of the galaxy and that make it rotate. [21](#)
- signal-to-noise ratio** Measure of the strength of the signal we want to detect and the background noise, which is undesired. [12](#)
- tilted-ring model** Kinematic model based on the assumption that the emitting material is contained in a thin disk, and that its motions are dominated by the rotation of the galaxy, and each ring at each radius has a constant circular velocity that only depends on its distance from the center. [12, 24](#)
- velocity map** Two-dimensional representation of stellar velocity and velocity dispersion obtained from calculating the Doppler effect on the regions of a galaxy, for example. [8](#)